Electronic Supplementary Material (ESI) for Journal of Materials Chemistry A.

Supporting Information for:

Electrochemical Neutralization Energy Assisted Low-Cost Acid-alkaline Electrolyzer for Energy-saving Electrolysis Hydrogen Generation

Yan Li[+], Junxiang Chen[+], Pingwei Cai, Zhenhai Wen*

CAS Key Laboratory of Design and Assembly of Functional Nanostructures, Fujian Provincial Key Laboratory of Nanomaterials, Fujian Institute of Research on the Structure of Matter, Chinese Academy of Sciences, Fuzhou, Fujian 350002, PR China

[+] These authors contributed equally to this work.

E-mail: wen@fjirsm.ac.cn

1. Experimental Details

1.1 Material preparation

Chemicals and Materials: Nickel (II) chloride hexahydrate puratrem ($NiCl_2$•$6H_2O$ ⩾98%), Polyvinylpyrrolidone (PVP K30) were purchased from GENERAL-REAGENT, phosphorus red purchased from Aladdin, Pt/C (20%) were bought from sigma-aldrich. All aqueous solutions were freshly acquired with high purity water (⩾18 MΩ cm) generated from a Gen Pure UV-TOC/UF ultra-pure water system (TKA, Niederelbert, Germany).

Synthesis of Ni_2P NR: 0.1 g Polyvinylpyrrolidone (PVP K30) was dissolved in 60 mL deionized water to form a uniform and clear solution at room temperature. Then, 5 mmol $NiCl_2$•$6H_2O$ was added with vigorous stirring for 10 min. 30 mmol phosphorus red were added into the solution. The mixture was transferred to the 100 mL Teflon-lined stainless steel autoclave and heated to 180 ºC for 15 hours. The resulting grey precipitates were collected by filter and washed with deionized water and ethanol several times and finally vacuum-dried at 80 ºC for 3 hour. The Ni_2P NP and Ni_2P NF were prepared with the same synthesis method of Ni_2P NR except using different dosage of PVP (0.05 g, 0.2 g)

1.2 Structural and surface characterization

Physical Measurements: X-ray photoelectron spectroscopy (XPS) was performed with a Phoibos 100 spectrometer and a Mg X-ray radiation source (SPECS Germany). The sample was homogeneously spread across on a carbon conductive tape for XPS analysis. Power X-ray diffraction (XRD) was conducted on a Bruker D8 advance diffractometer at 40 mA and 40 KV, using Cu Kα (λ= 1.5418Å) radiation. Transmission electron microscopy (TEM) was performed on a JEM-2100 UHR microscope (JEOL, Japan) at an accelerating voltage of 200 kV with an attached selected area electron diffraction (SAED) and energy-dispersive X-ray spectroscopy (EDS). High resolution field emission scanning electron microscope was conducted on a Field Emission Scanning Electron Microscope, FESEM (SU-8010) used to obtain SEM images. Specific surface area, pore volume and pore size distribution of the products was examined by the Brunauer-Emmett-Teller (BET) method using nitrogen adsorption and desorption isotherms on an Intelligent Gravimetric Sorption Analyser (IGA100B).

1.3 Electrochemical Measurements

HER and OER, electrochemical experiments were performed on a CHI 760 electrochemical analyzer (Shanghai, China) in a standard three-electrode system using a glassy carbon electrode (GCE) with various catalysts as the working electrode, platinum electrode as the counter electrode, and Ag/AgCl as reference electrode. The working electrode was prepared as follows: 5 mg catalytic materials, 50 μL Nafion and 30 μL ethanol were suspended in 420 μL water and sonicated for 30 min to form homogeneous ink. Then 6 μL of ink was dropped onto the surface of glassy carbon electrode and dried at room temperature. The resulting catalyst loading was 0.429 mg cm^{-2}. For HER measurements, the commercial Pt/C (20% Pt) modified electrode was prepared as the same method for comparison. Measurements of activity for hydrogen evolution reaction (HER) were performed in 0.5 M H_2SO_4, 1.0 M KOH and 0.1 M phosphate buffer saline solution (PBS, PH=7.32) using a variety of electrochemical techniques. For Oxygen evolution reaction (OER) measurements, 1.0 M KOH was used as the electrolyte. The catalyst was cycled 30 times by CV until a stable CV curve was obtained before testing. All CV curves presented here were not corrected for iR losses. The reference electrode was calibrated to reversible hydrogen potential (RHE) using platinum electrode for both working and counter electrodes in the same electrolyte, and converted to RHE according to the Nernst equation (ERHE=$E_{Ag/AgCl}$+ $E_{Ag/AgCl}$ + 0.0591pH). While for overall water splitting with bipolar membrane, the Ni_2P electrodes were prepared by dispersing 80 wt. % Ni_2P powder, 10 wt. % carbon black and 10 wt. % PVDF binder in n-methyl-pyrrolidone (NMP) solvent to form homogeneous slurry. The slurry was spread on carbon cloth substrates with 1.0 cm^2 in area (Figure S18) and then dried at 80 °C overnight under vacuum. A tailor-made glass water-splitting cell was used to fix the prepared catalyst electrodes and bipolar membrane. A commercial bipolar membrane was used to separating anode and cathode in water-splitting cell. The cell with anodic compartments filled with 1 M KOH solution and cathodic compartment filled with 0.5 M H_2SO_4.

1.4 Electrochemical active surface area (ECSA)

The capacitive currents are measured in a potential range where no faradic processes occured. We sweep the potential between 0.10 to 0.20 V *vs.* RHE for thirty cycles at different scan rates (10, 20, 40, 60, 80, 100, 120, 140, 160, 180 and 200 mV s^{-1}). The differences in current density variation ($\Delta j= j_a - j_c$) at the potential of 0.15 V *vs.* RHE plotted against scan rate are fitted to estimate the electrochemical double-layer capacitances (C_{dl}), which are used to estimate the electrochemical surface area (ECSA).

1.5 Turnover frequency (TOF) calculations

The TOF is defined as the number of H_2 or O_2 molecules evolved per site per second:

TOF = j / nFN[1]

where j is the measured current density (mA cm^{-2}), n is the mole number of electrons per mole of H_2 or O_2, F is the Faraday constant (96485 C mol^{-1}), and N is the Ni content (mol cm^{-2}).

1.6 Faradaic efficiency calculation

Faradaic efficiency of water splitting catalyzed by Ni_2P NR was calculated by dividing the amount of the experimentally generated gas by the theoretical amount of gas which is calculated by the charge passed through the electrode:

(1) $\text{Faradaic efficiency}_{H2} = V_{\text{experiment}} / V_{\text{theoretical}} = V_{\text{experiment}} / [(2/4)*(Q/F)*V_m]$

(2) $\text{Faradaic efficiency}_{O2} = V_{\text{experiment}} / V_{\text{theoretical}} = V_{\text{experiment}} / [(1/4)*(Q/F)*V_m]$

where Q is the summation of the charge passed through the electrodes, F is the Faraday constant (96485 C mol^{-2}), the number 4 means 4 moles of electrons per mole of H_2O, the number 2 means 2 moles of H_2 per mole of H_2O, the number 1 means 1 moles of O_2 per mole of H_2O and V_m is the molar volume of gas (24.1 L mol^{-1}, 293 K, 101 kPa).

2. Supplementary Figures

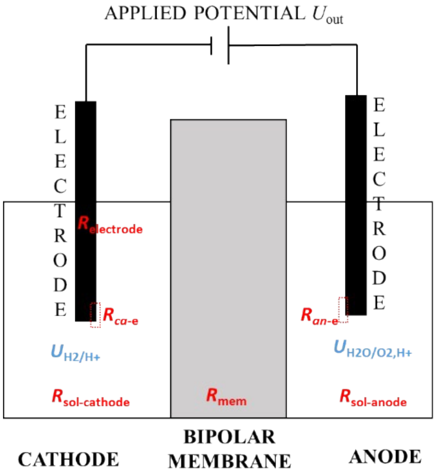

$R_{electrode}$= Resistance of electrode
$R_{ca\text{-}e}$= Resistance caused by cathodic reaction
$R_{an\text{-}e}$= Resistance caused by anodic reaction
R_{mem}= Resistance of the bipolar membrane
$R_{sol\text{-}cathode}$= Resistance of the solvation on cathode
$R_{sol\text{-}anode}$= Resistance of the solvation on anode
$U_{nominal}$=Nominal Voltage
$U_{nominal}(\Delta pH=0)$=Nominal Voltage when there is no pH differences
$U_{A/B}$=Potential (vs SHE) of the associated A/B couple

$$U_{nominal}=U_{H2O/O2,H+}-U_{H2/H+}$$
$$=U_{nominal}(\Delta pH=0)-0.059\,(pH_{cathode}-pH_{anode})$$

$$U_{out}=U_{nominal}+i(R_{electrode}+R_{ca\text{-}e}+R_{an\text{-}e}+R_{mem}+R_{sol\text{-}cathode}+R_{sol\text{-}anode})$$

Figure S1. The scheme of the system we study in this paper, where the associated fundamental electrochemistry is displayed.

From thermodynamics, the half-cell and total reactions of each separate electrode sides, together with electrode potential dependence on pH are described as below:

$$2H^{+} + 2e^{-} \leftrightarrow H_2 \tag{1}$$

$$E_{H^{+}/H_2} = E^{0}_{H^{+}/H_2} + \frac{RT}{nF} ln \left[\frac{\alpha_{H_2}}{\left(a_{H^{+}}\right)^{2}} \right] = 0\ V - 0.059 \times pHC \tag{2}$$

$$4OH^{-} - 4e^{-} \leftrightarrow O_2 + 2H_2O \tag{3}$$

$$E_{O_2/OH^{-}} = E^{0}_{O_2/OH^{-}} + \frac{RT}{nF} ln \left[\frac{\alpha_{O_2}\left(\alpha_{H_2O}\right)^{2}}{\left(\alpha_{OH^{-}}\right)^{4}} \right] = 1.229\ V - 0.059 \times pHA \tag{4}$$

$$4H^{+} + 4OH^{-} \leftrightarrow H_2 + O_2 \tag{5}$$

$$E_t = E_{O_2/OH^{-}} - E_{H^{+}/H_2} = 1.229V - 0.059 \times \Delta pH \tag{6}$$

where E is the half-cell potential, E^0 is the standard half-cell potential, R is the universal gas constant, T is the absolute temperature at which the cell is operated, F is the Faraday constant, n is the number of moles of electrons transferred in the half-reaction, α is the chemical activity for the relevant species, ΔpH is the $pH_A - pH_C$. E_t is the theoretical potential of water electrolysis.

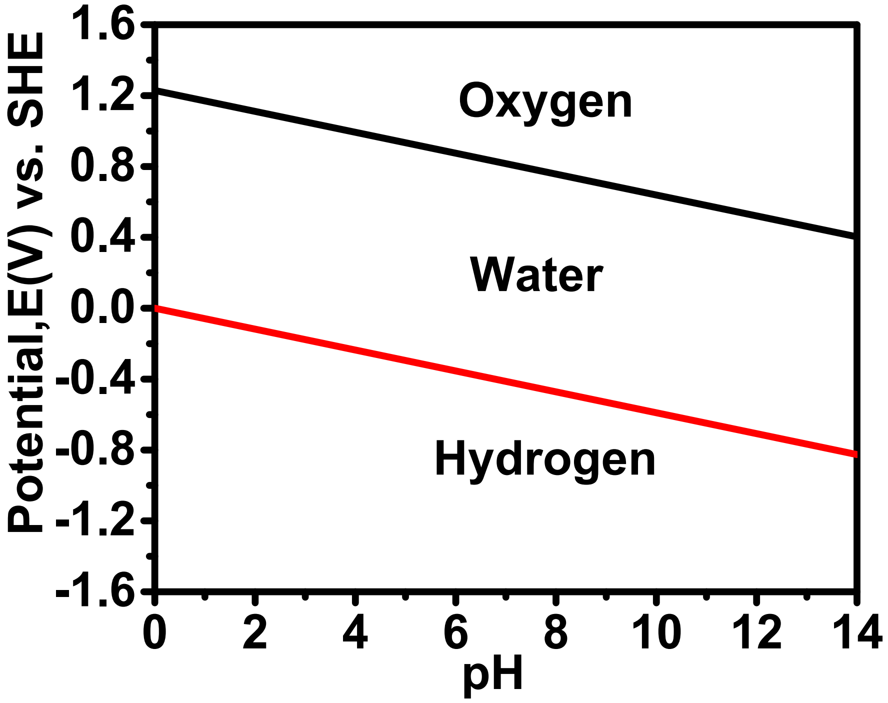

Figure S2. Pourbaix diagram of water with curves generated by the Nernst equation.

According to equations (1-6) and Figure S2, the potential of the electrodes remains a constant of 1.229 V， the maximum potential of water splitting, when the pH value is independent of the electrolyte ($pH_C = pH_A$). At this point, the theoretical eletrolysis power is also maximal. Once $pH_C \neq pH_A$, the E_t will be changed owing to the neutralization of pH different solutions, i.e., the Oxygen electrode in alkaline (pH=14) and hydrogen electrode in acid (pH=0), the voltage for water electrolysis can be reduced to 0.403 V.

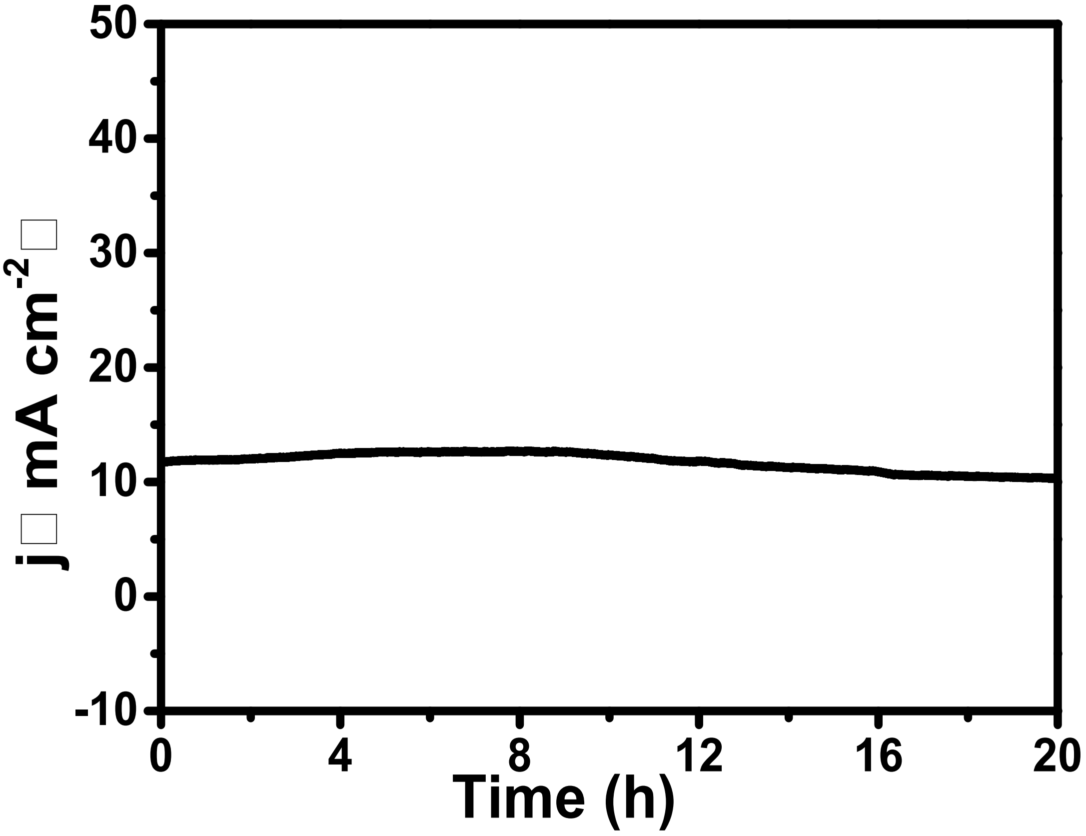

Figure S3. Change of current density during the water-splitting electrocatalysis at applied voltage of 1.2 V.

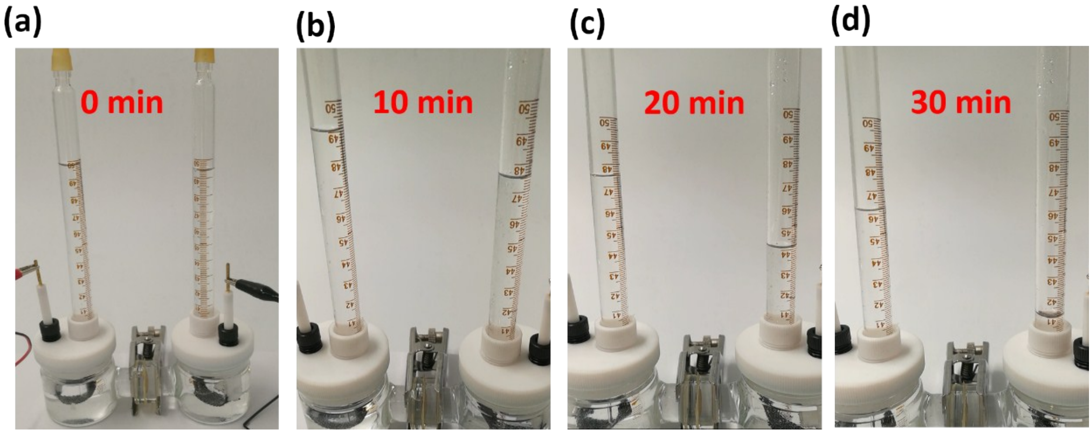

Figure S4. Digitals of bipolar membrane water-splitting device powered by AA battery of 1.5 V at different time, (a) 0 min, (b) 10 min, (c) 20 min, (d) 30 min.

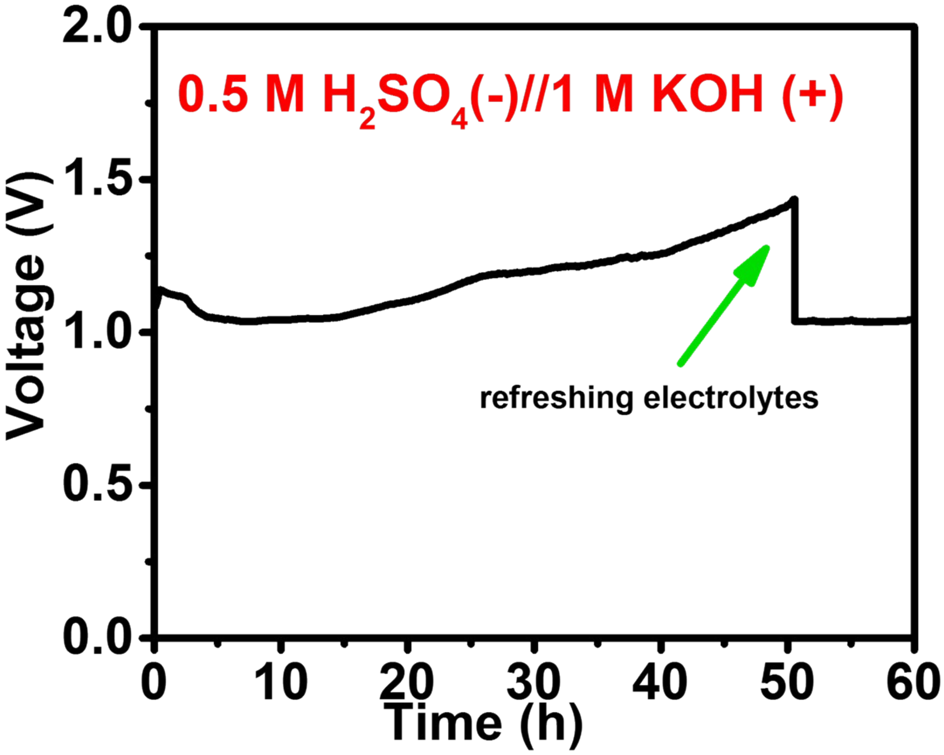

Figure S5. Voltage monitor of the bipolar membrane water-splitting electrolyzer with continuous running at a constant current density of 10 mA cm^{-2}.

We also tested the stability of the present BPM water-splitting electrolyzer by monitoring the voltage variation running at a fixed current density of 10 mA cm^{-2}, during which the pH of both anolyte and catholyte were recorded. In the initial 20 hours, there is no significant variation in both voltage and pH. With time going on, the applied voltage and the pH value in catholyte start to rise with decreasing of the pH value in anolyte. The applied voltage increase to 1.5 V over 50 hours running, while the applied voltage decrease back to ~1.12 V when refreshing electrolyte. This result indicates that the continuous consumption of H$^+$ and OH$^+$ in cathode and anode, respectively, and the pH-gradient between in the BPM water-splitting electrolyzer do assist water splitting with reducing the applied voltage.

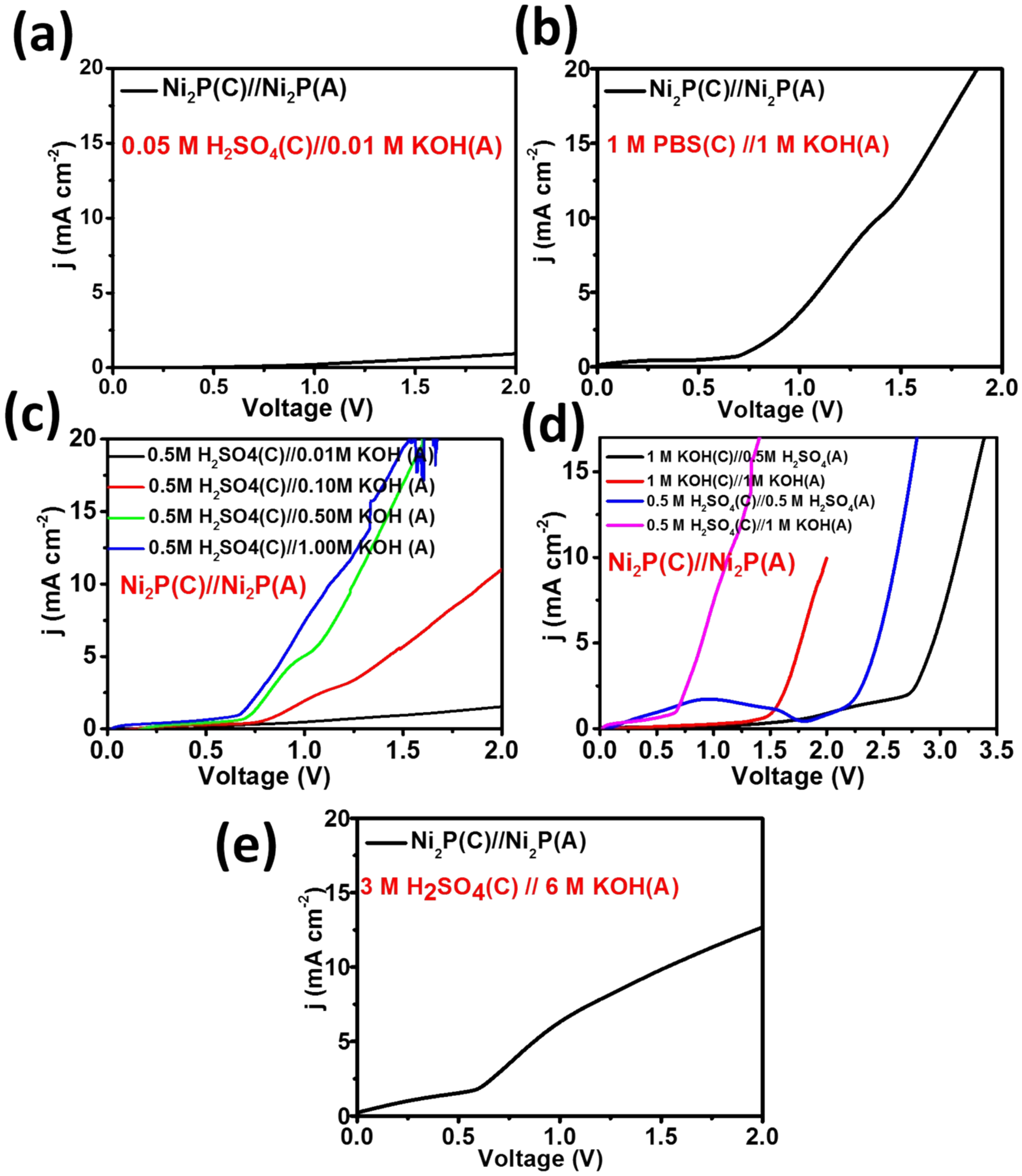

Figure S6 (a)-(e). Linear sweeping voltammetry for different water-splitting electrolyzer with Ni_2P NR as anode and cathode containing different electrolyte.

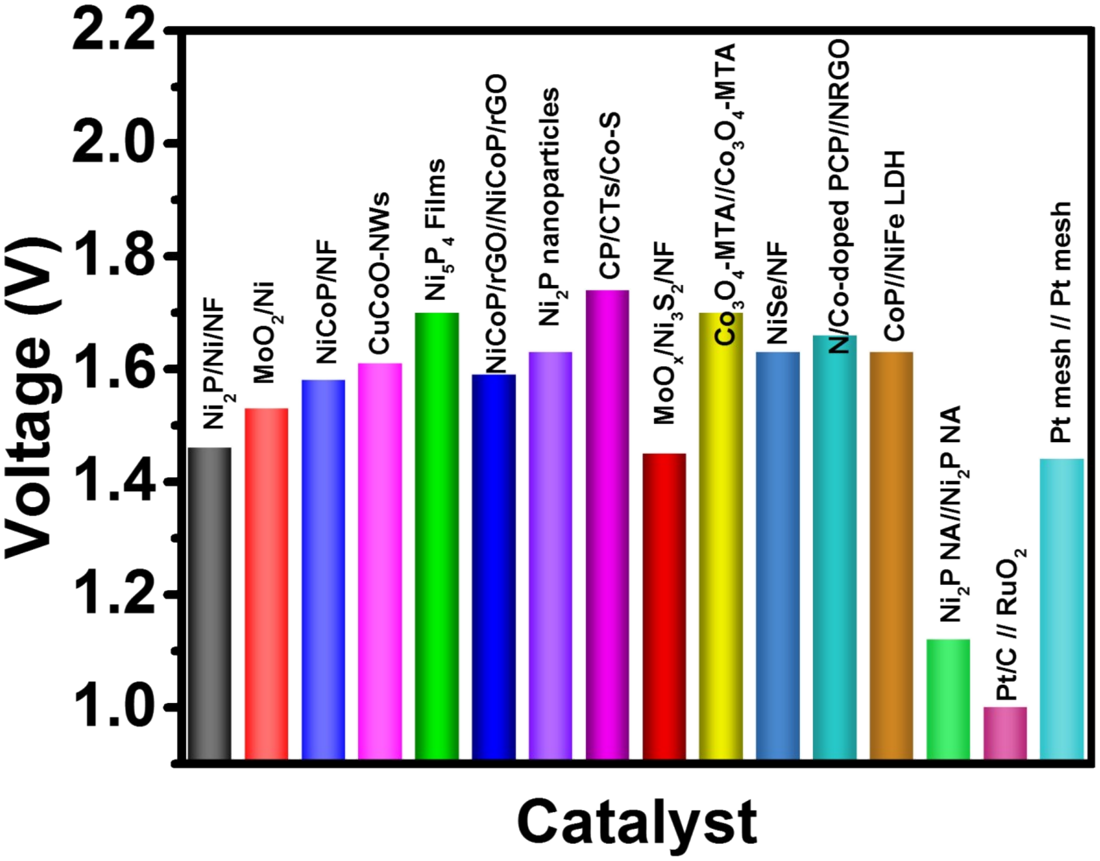

Figure S7. The applied voltage to achieve a current density of 10 mA cm^{-2} for the present electrolyzer (Ni_2P // Ni_2P, Pt/C // RuO_2, Pt mesh // Pt mesh) and the previous electrolyzer running in alkaline solution.

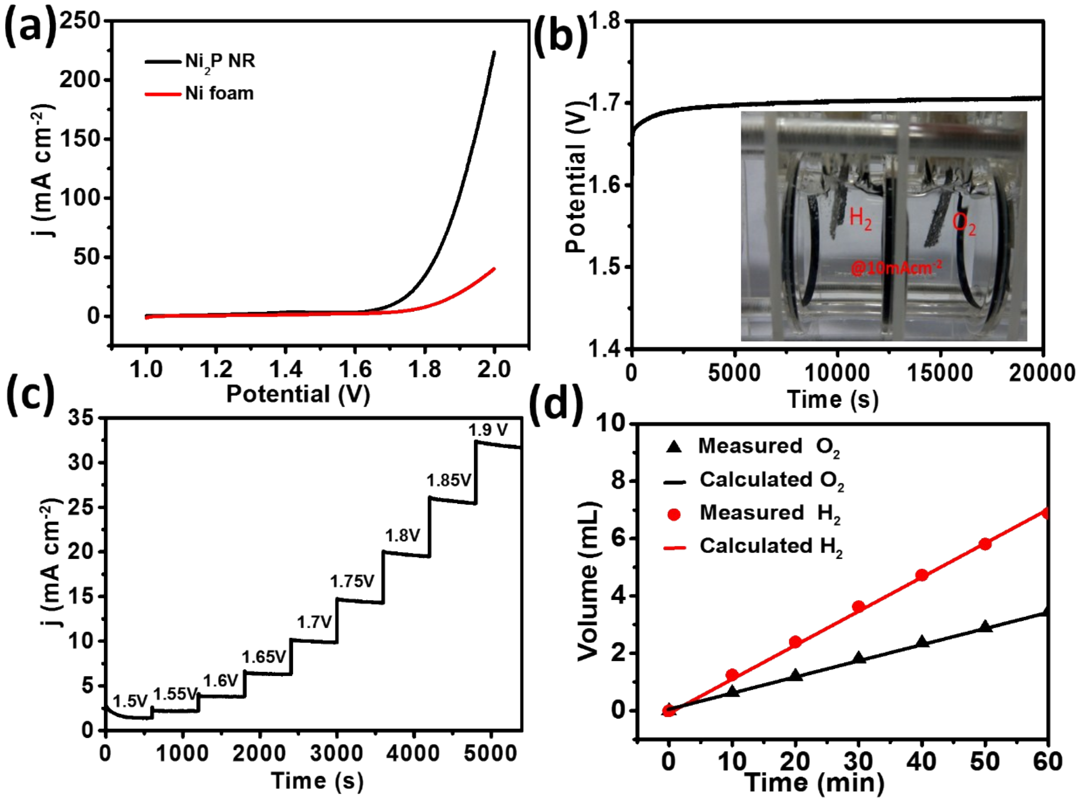

Figure S8. (a) Linear sweeping voltammetry curve of an alkaline electrolyzer using Ni_2P NR as anode and cathode catalyst (Support: Ni foam; loading of catalyst: 3.6 mg cm^{-2}; electrolyte: 1M KOH.). (b) Galvanostatic electrolysis in 1 M KOH at a constant current density of 10 mA cm^{-2} over 20000 s, and the corresponding digital photograph of two-electrode water splitting electrolyzer in an alkaline electrolyzer with Ni_2P NR as both anode and cathode. (c) Multistep chronoamperometric curve obtained with Ni_2P NR in 1 M KOH solution, measured at different overpotentials, starting at 1.5 V and ending at 1.9 V with an increment of 50 mV every 600 s. (d) The amount of gas theoretically calculated and experimentally measured versus time for overall water splitting of Ni_2P NR.

The Ni_2P NR was applied as both anode and cathode for water electrolysis with a 1.0 M KOH as catholyte and anolyte. An applied voltage about 1.70 V is required to achieve a current density of 10 mA cm^{-2} (Figure S8a). The fairly stable bearing potential was input at J = 10 mA cm^{-2} and the considerable H_2 and O_2 bubbles were produced at corresponding electrodes during a 20000 s galvanostatic electrolysis experiment (Figure S8b and its inset). Figure S8c shows a multi-step chronoamperometric curve with an increment of 50 mV every 600 s for water splitting over the above electrolyzer. The results reveal that the catalytic current density operates stably and switches rapidly in a wide range of applied potential from 1.5 V to 1.9 V. The volume–time curves (Figure S8d) for the amount of experimentally quantified H_2 and O_2 match theoretically calculated gas, indicating the Faradaic efficiency is nearly 100 % for electrocatalytic overall water splitting with the ratio of O_2 and H_2 being close to 1:2. Although the stability and Faradaic efficiency of this system are very high, while the voltage required delivering 10 mA cm^{-2} is around 1.5 times of that of BPM-assisted water-splitting device. The result indicating Ni_2P NR presents higher activity in the pH-gradient concentration cell than in single electrolyte.

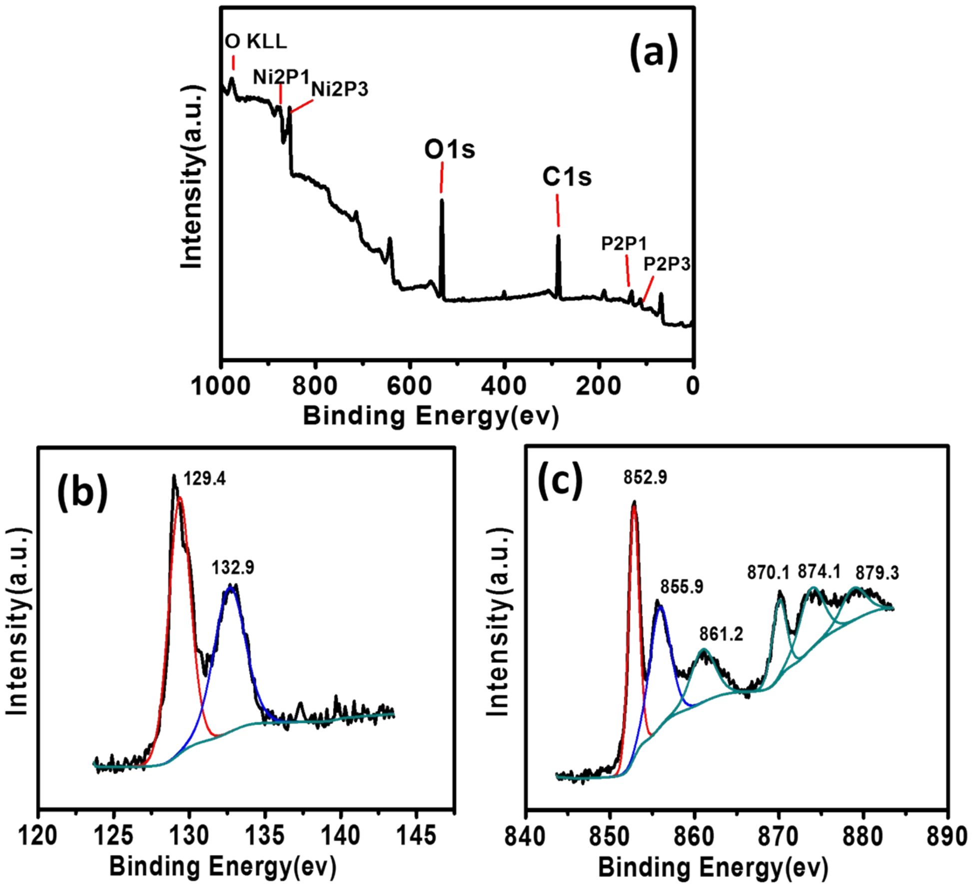

Figure S9. (a) Survey XPS spectra of Ni_2P NR, high-resolution spectra for (b) Ni 2p, and (c) P 2p

The surface chemical compositions and states of Ni_2P NR was investigated by X-ray photoelectron spectra (XPS; Figure S4a-c,). Three peaks for Ni 2p 3/2 energy level, *i.e.*, 852.9, 855.9 and 861.2 eV, can be assigned to $Ni^{\delta+}$ in Ni_2P, oxidized Ni species, and the satellite of Ni 2p 3/2 peak, respectively. In addition, three peaks are observed at around 870.1, 874.1 and 879.3 eV due to the Ni 2p 1/2 energy level, which are attributed to $Ni^{\delta+}$ in Ni_2P, oxidized Ni species and the satellite of Ni 2p 1/2 peak, respectively.[2] The P 2p spectrum exhibits two peaks at around 129.4 and 132.9 eV, reflecting the binding energy of P 2p1/2 and P 2p3/2, respectively.[3] The peaks at 855.9 and 132.9 eV can be assigned to oxidized Ni and P species arising from superficial oxidation of Ni_2P due to air contact.[4, 5] The Ni (2p) binding energy of

852.9 eV is positively shifted from that of Ni metal, while the P (2p) binding energy of 129.4 eV is negatively shifted from that of elemental P[2], suggesting that Ni and P have partial positive (δ+) and negative (δ-) charges with a transfer of electron density from Ni to P occurs.[6]

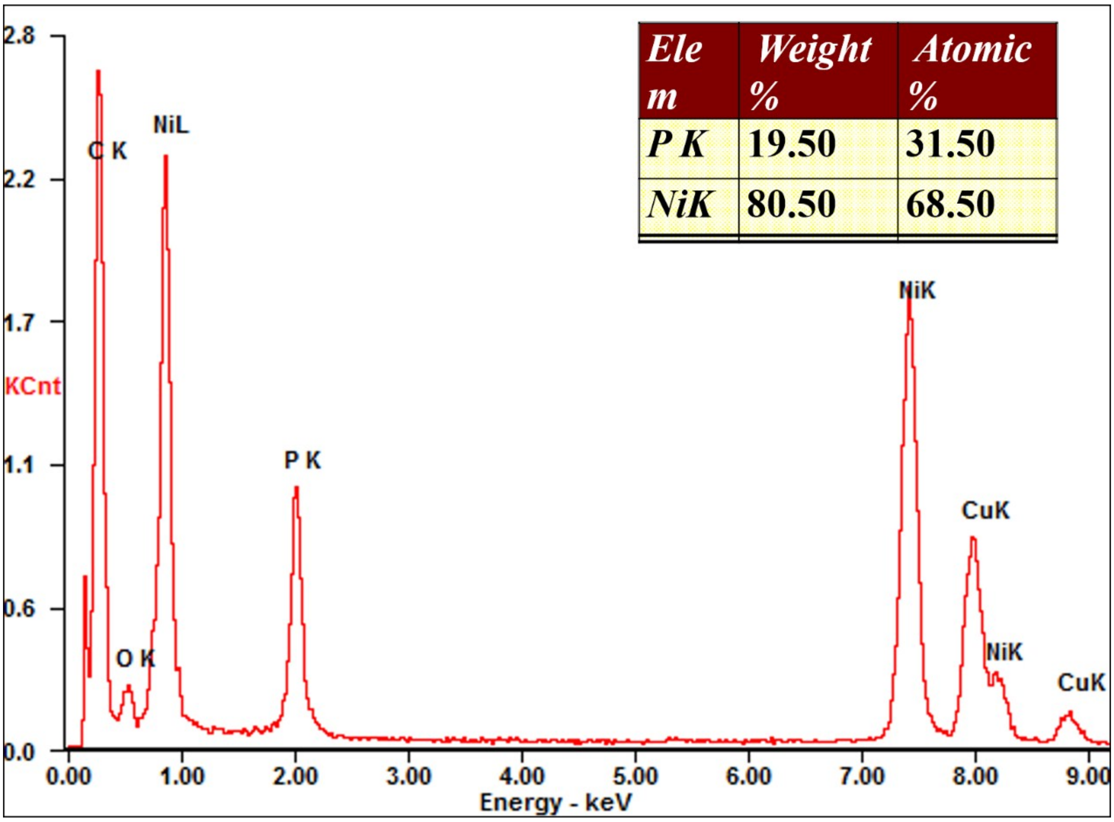

Elem	*Weight %*	*Atomic %*
P K	19.50	31.50
NiK	80.50	68.50

Figure S10. EDS spectrum of the Ni_2P NR

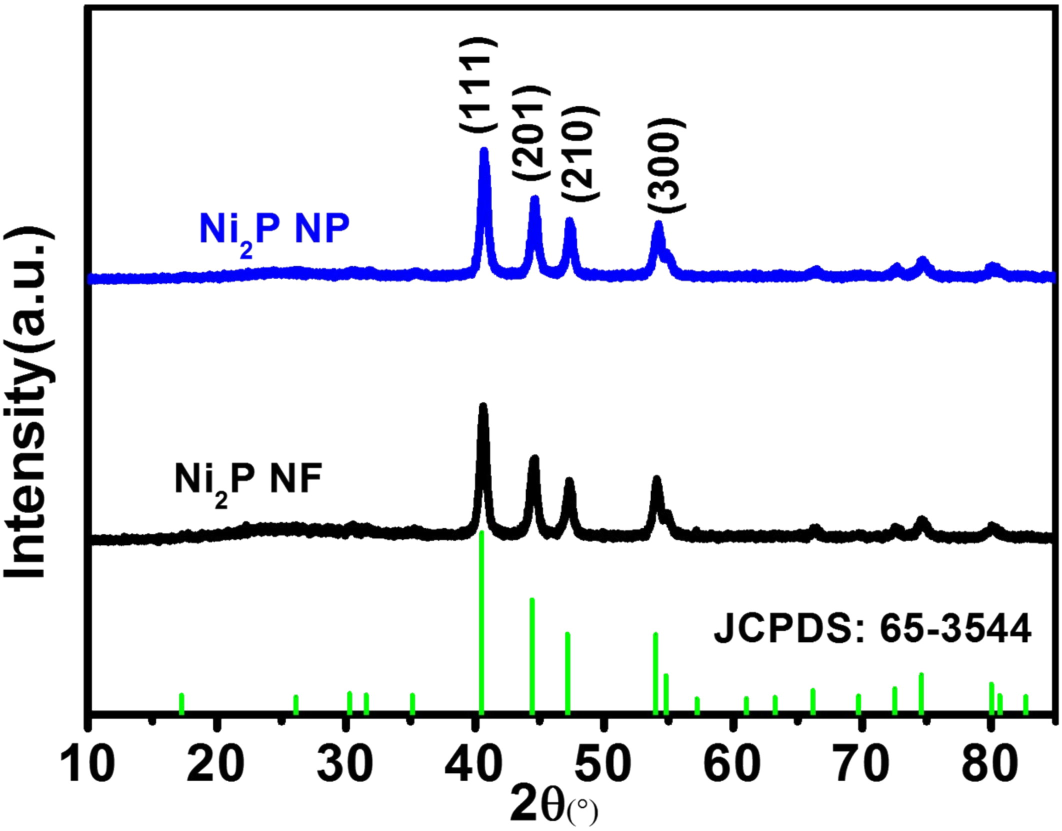

Figure S11. Powder XRD patterns of Ni_2P NP and Ni_2P NF.

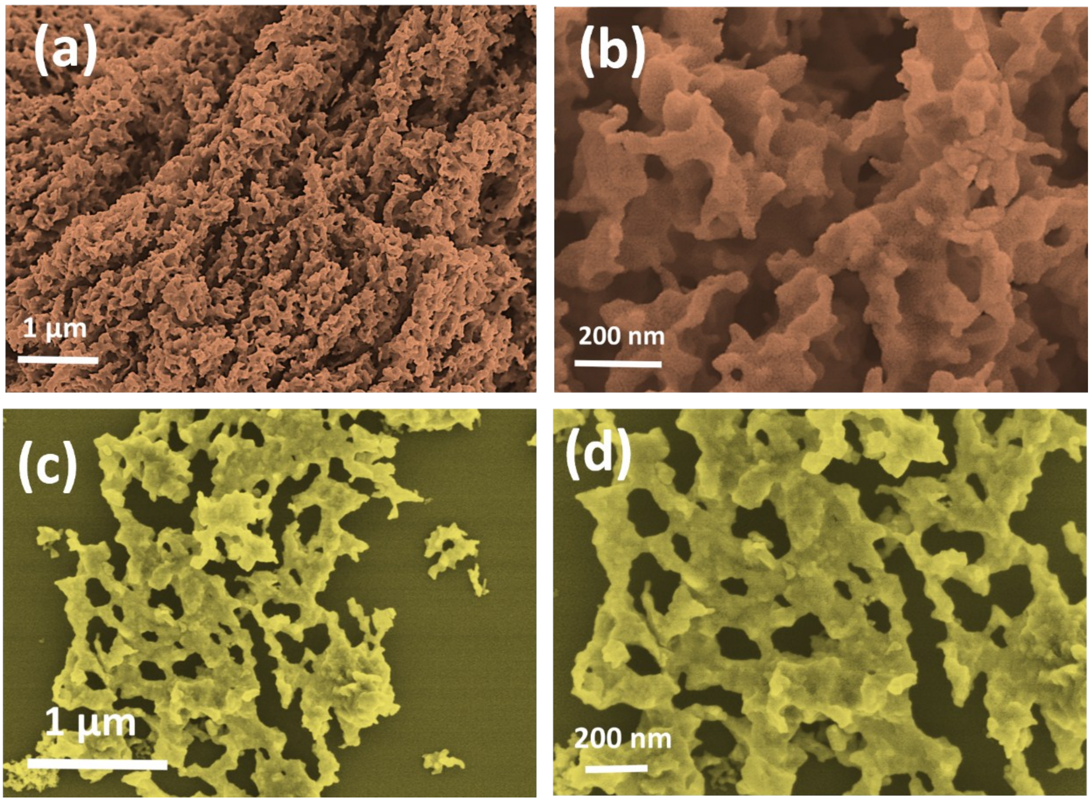

Figure S12. Low- and high-magnified SEM images of Ni_2P NP (a-b), Ni_2P NF (c-d).

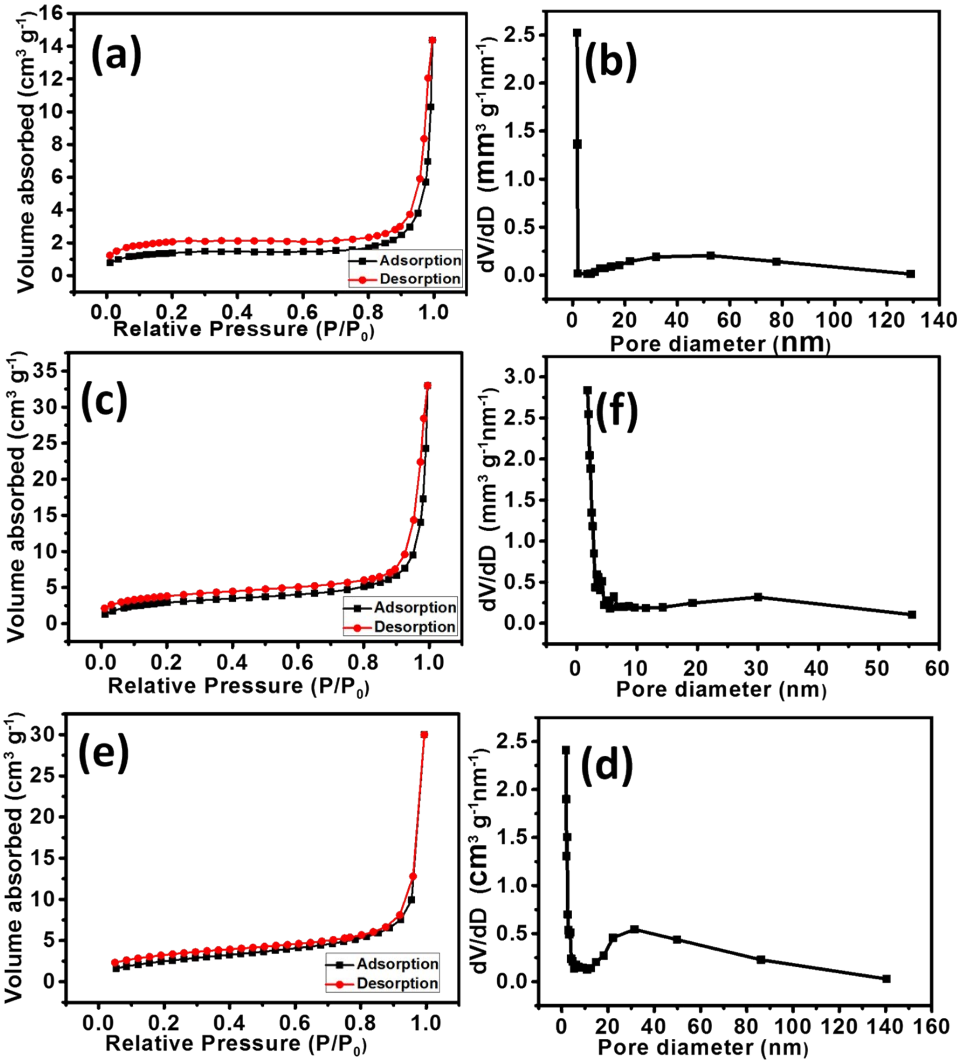

Figure S13. N_2 adsorption–desorption isotherms for samples of (a) Ni_2P NP, (c) Ni_2P NR, and (e) Ni_2P NF; the corresponding pore size distribution for samples of (b) Ni_2P NP, (d) Ni_2P NR, and (f) Ni_2P NF.

Due to the porous 3D structure and ultrafine nanorods, the Ni_2P NR possess a Brunauer-Emmett-Teller (BET) surface area of about 44.97 m^2 g^{-1}; this value is almost 10 and 5 times larger than those of Ni_2P NP (4.68 m^2 g^{-1}) and Ni_2P NF (9.39 m^2 g^{-1}) (Figure S14), indicating the porous nanorods structure contributes to a significantly improved surface area.

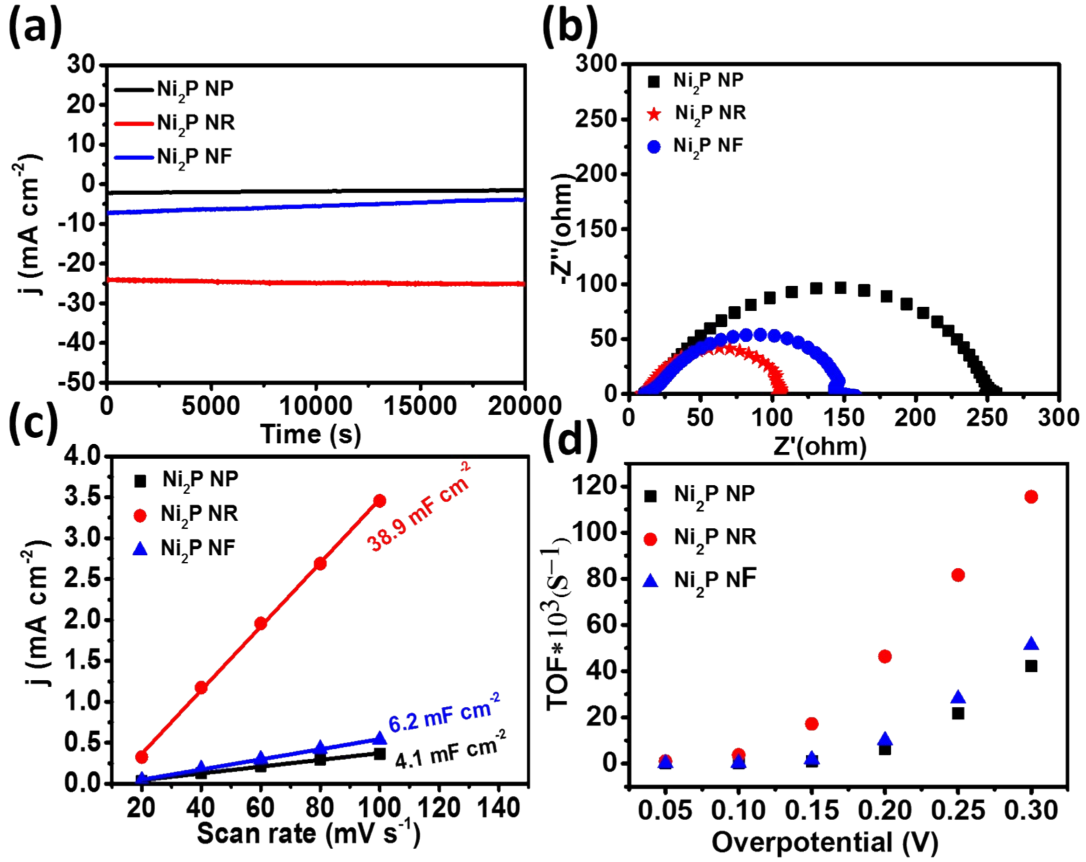

Figure S14. Electrocatalysis for hydrogen evolution reaction in 0.5 M H_2SO_4. (a) Time-dependent current density curve for Ni_2P NP, Ni_2P NR, Ni_2P NF at an applied voltage of -0.15 V *vs.* RHE; (b) Nyquist plots of Ni_2P NP, Ni_2P NR, Ni_2P NF with an applied voltage of -0.103 V *vs.* RHE; (c) Slope derived from current density plotted against scan rate showing the extraction of the double-layer capacitances; (d) H_2 turn over frequencies (TOFs) per surface site over different catalysts.

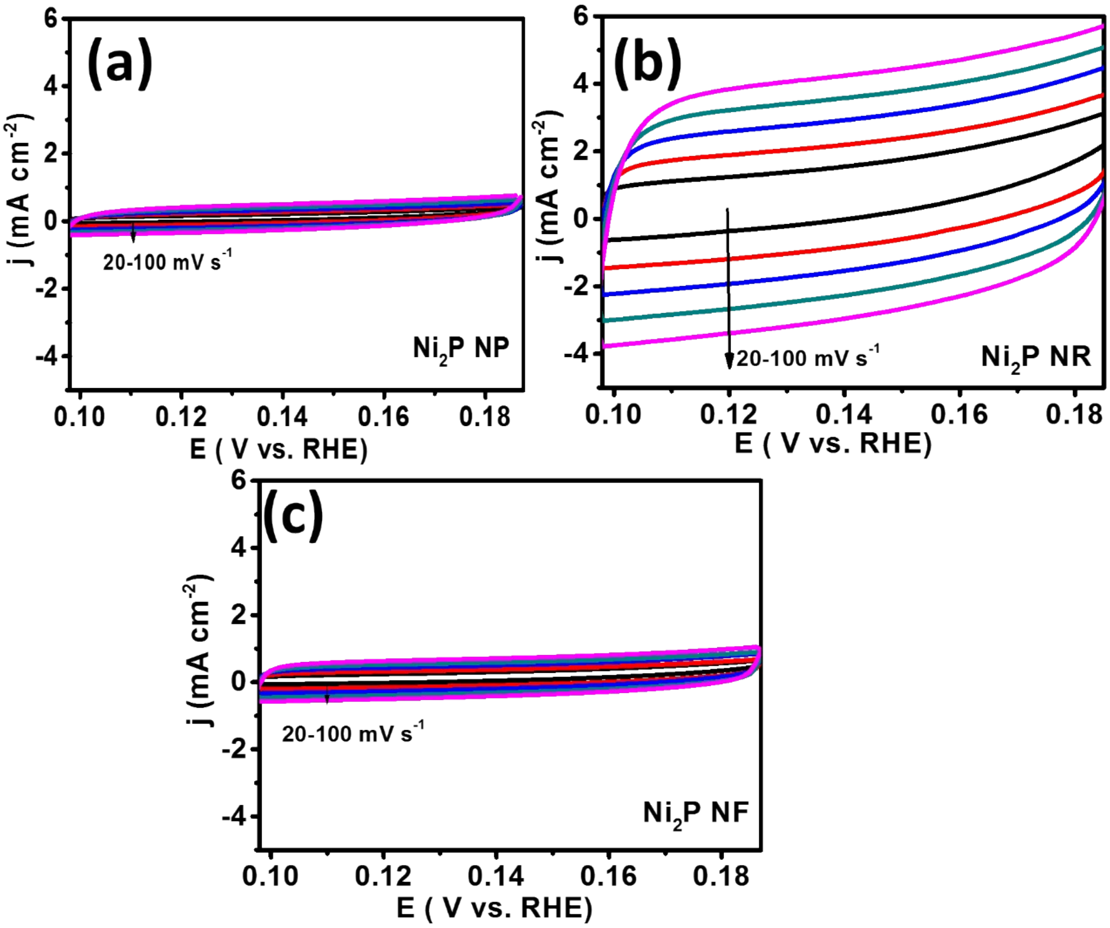

Figure S15. Electrochemical capacitance measurements for the estimation of the electrochemical active surface area of catalysts; Cyclic voltammograms of the (a) Ni_2P NP, (b) Ni_2P NR, (c) Ni_2P NF modified electrode at various scan rates.

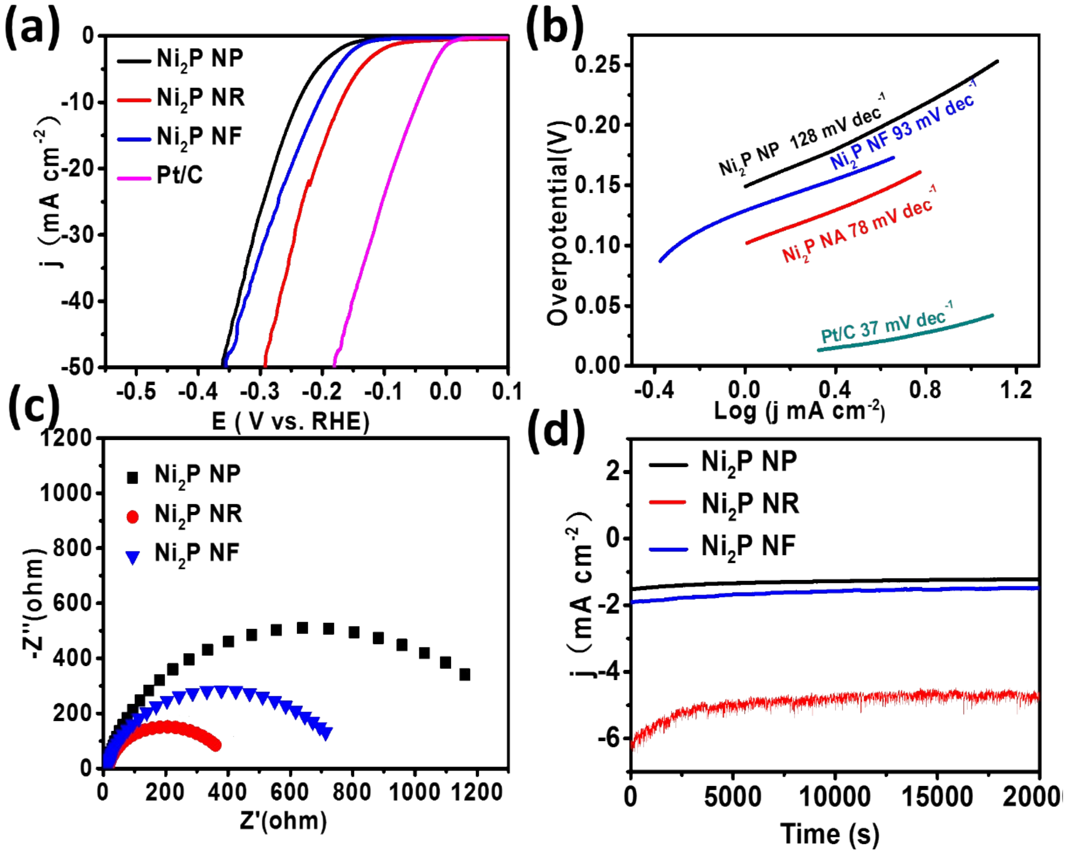

Figure S16. Hydrogen evolution reaction electrocatalysis in 1 M KOH. (a) Polarization curves for the Ni_2P NR recorded at a scan rate of 5 mV s^{-1}, along with Ni_2P NP, Ni_2P NF, and Pt/C for comparison; (b) Tafel slopes for the corresponding electrocatalysts; (c) Time-dependent current density curve for Ni_2P NR at -0.15 V vs. RHE. (d) Nyquist plots of Ni_2P NR in 1.0 M KOH with the potential of -0.147 V versus RHE.

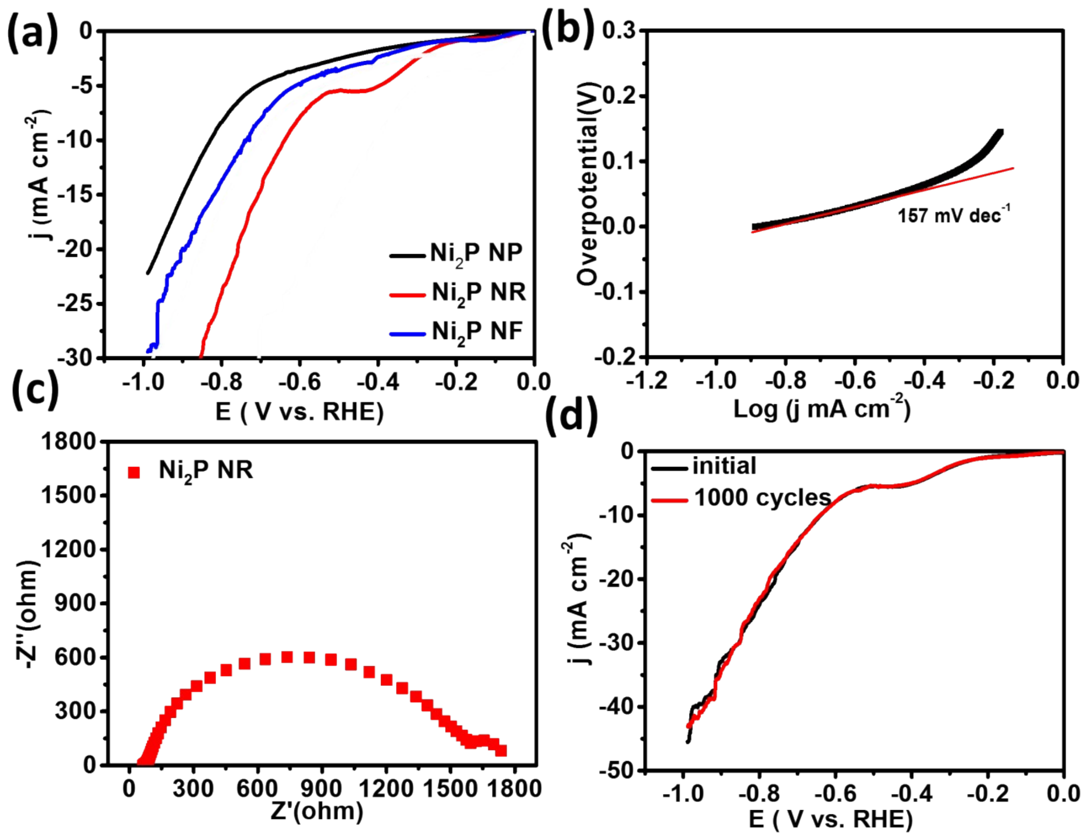

Figure S17. (a) Polarization curves for Ni_2P NP, Ni_2P NR Ni_2P NF at a scan rate of 5 mV s^{-1} in 0.1 M PBS; (b) Tafel plots (c) Electrochemical impedance spectra at -0.300 V *vs*. RHE for Ni_2P NR in 0.5 M PBS; (d) Polarization data for Ni_2P NR in 0.1 M PBS for initially and after 1000 CV sweeps.

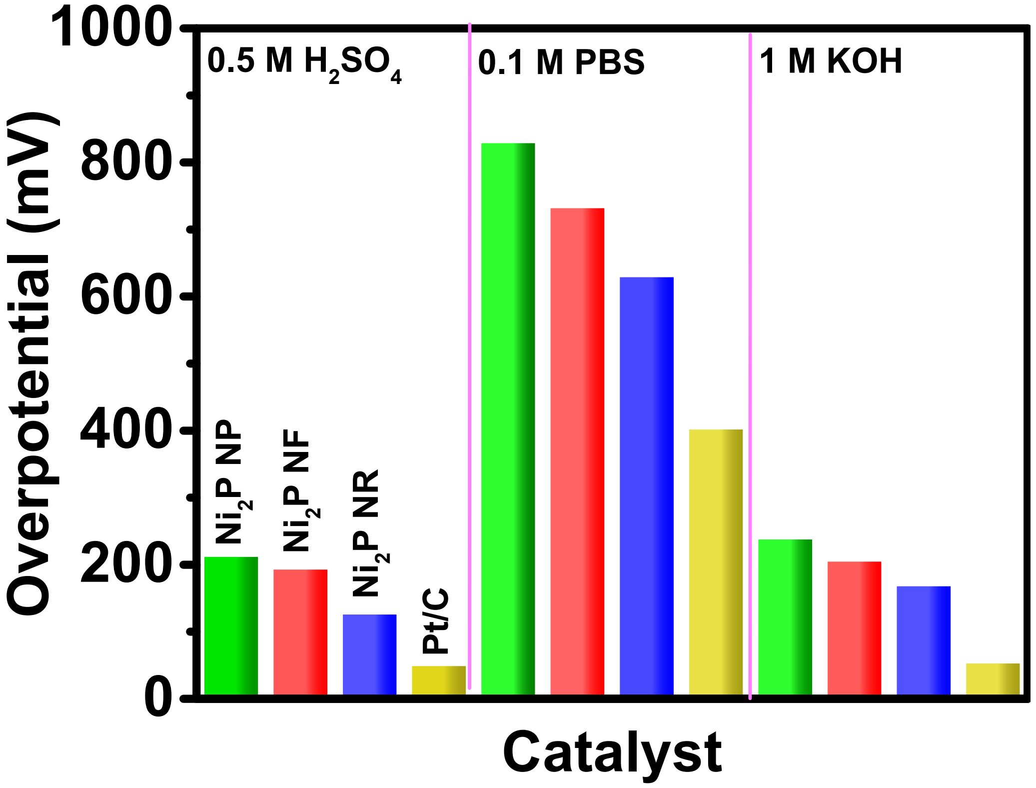

Figure S18. Overpotentials to release of 10 mA cm^{-2} of various electrodes in 0.5 M H_2SO_4, 0.1 M PBS, 1.0 M KOH**.**

In 0.5 M H_2SO_4, the overpotential gap between Pt/C and Ni_2P NF is around 77 mV, while the overpotential gaps in 0.1 M PBS and 1.0 M KOH is 200 mV and 115 mV, respectively, implying that the Ni_2P NR HER electrocatalyst perform the best in 0.5 M H_2SO_4.

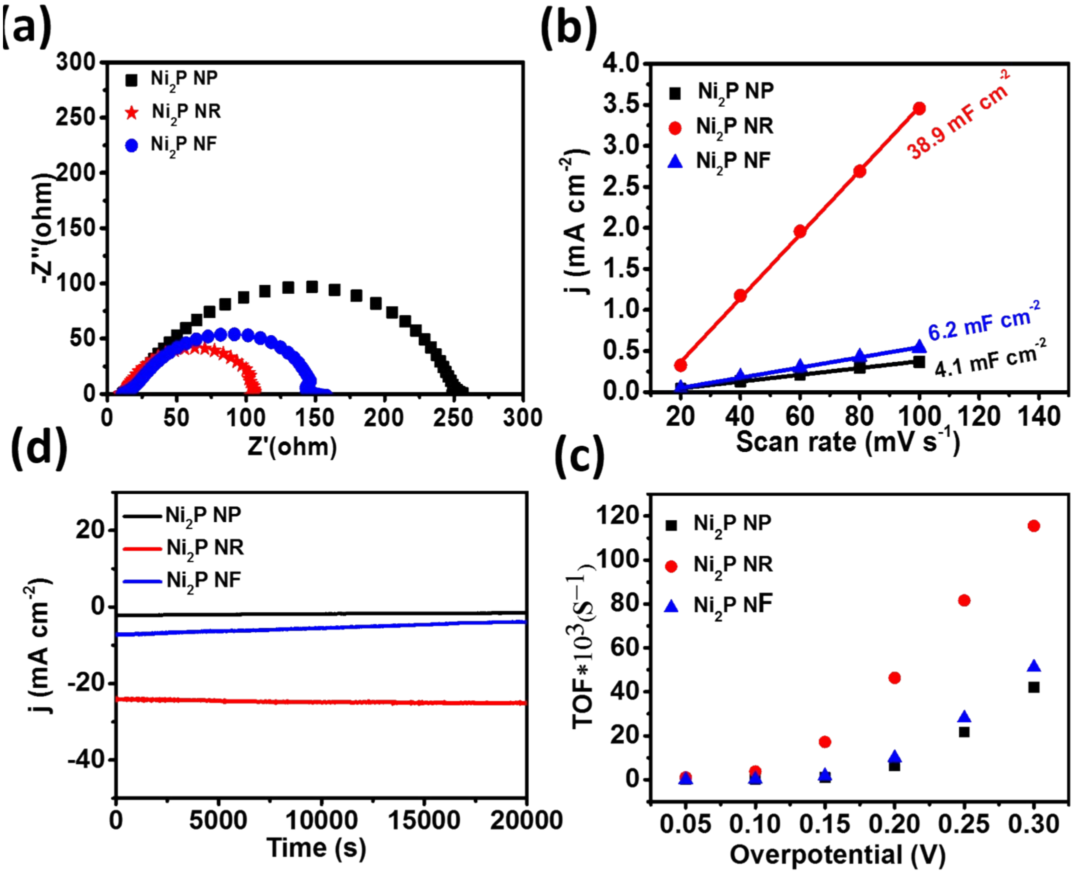

Figure S19. Electrocatalysis of oxygen evolution reaction for Ni_2P NP, Ni_2P NR, and Ni_2P NF in 1.0 M KOH. (a) Time-dependent current density curve for Ni_2P NR at 1.57 V *vs*. RHE; (b) Nyquist plots; (c) Slope derived from current density plotted against scan rate showing the extraction of the double-layer capacitances; (d) turn over frequencies (TOFs) per surface site for O_2 over different catalysts.

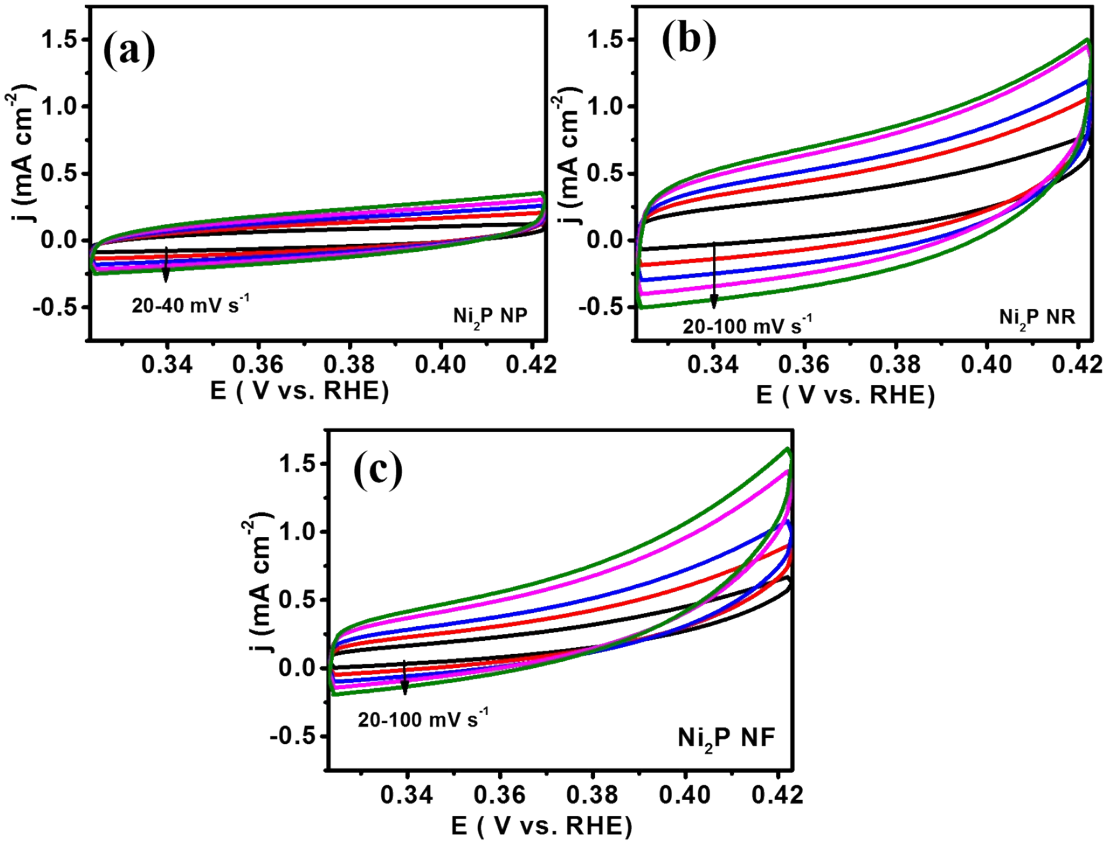

Figure S20. Electrochemical capacitance measurements for the estimation of the relative electrochemical active surface area of catalysts upon OER. Cyclic voltammograms of the electrodes for (a) Ni_2P NP, (b) Ni_2P NR, (c) Ni_2P NF at various scan rates.

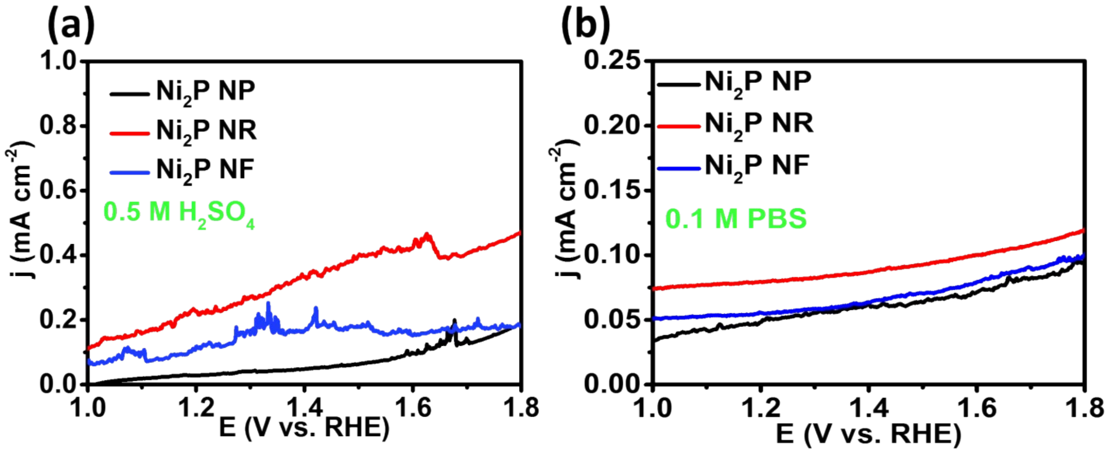

Figure S21. LSV curves of OER over Ni_2P NP, Ni_2P NR and Ni_2P NF catalysts in (a) 0.5 M H_2SO_4 and (b) 0.1 M PBS. One can see that all the Ni_2P samples show poor catalytic activity toward OER.

3. Supplementary Tables

Table S1. Comparison of water-splitting performance in optimal condition of Ni_2P NA with some representative water-splitting catalysts in alkaline condation

Catalysts	Electrolyte	E_{10} (V)	Ref
Ni_2P/Ni/NF	1 M KOH	1.49	7
MoO_2/Ni	1M KOH	1.53	8
NiCoP/NF	1M KOH	1.58	9
CuCoO-NWs	1M KOH	1.61	10
Ni_5P_4 Films	1M KOH	1.7	11
NiCoP/rGO‖NiCoP/rGO	1M KOH	1.59	12
Ni_2P nanoparticles	1M KOH	1.63	13
CP/CTs/Co-S	1M KOH	1.743	14
MoOx/Ni_3S_2/NF	1M KOH	1.45	15
Co_3O_4-MTA//Co_3O_4-MTA	1M KOH	1.70	16
NiSe/NF	1M KOH	1.63	17
N/Co-doped PCP//NRGO	0.1M KOH	1.66	18
CoP cathode	0.5M H_2SO_4	1.63	19
NiFe LDH anode	1M KOH		
Ni_2P NR cathode	**0.5M H_2SO_4**	**1.13**	**This work**
Ni_2P NR anode	**1.0 M KOH**		

Table S2. The pH value of different electrolyte bipolar membrane water-splitting system

Anode material	**Anode solution**	**Anode PH**	**Cathode material**	**Cathode solution**	**Cathode PH**
Ni_2P NR	1M KOH	14.12	Ni_2P NR	0.5M H_2SO_4	0.45
Ni_2P NR	0.5M KOH	13.81	Ni_2P NR	0.5M H_2SO_4	0.45
Ni_2P NR	0.1M KOH	13.19	Ni_2P NR	0.5M H_2SO_4	0.45
Ni_2P NR	0.01M KOH	12.21	Ni_2P NR	0.5M H_2SO_4	0.45
Ni_2P NR	1M KOH	14.12	Ni_2P NR	1M KOH	14.12
Ni_2P NR	0.5M H_2SO_4	0.45	Ni_2P NR	0.5M H_2SO_4	0.45
Ni_2P NR	0.5M H_2SO_4	0.45	Ni_2P NR	1M KOH	14.12
Ni_2P NR	0.05M H_2SO_4	2.45	Ni_2P NR	0.01M KOH	12.20
Ni_2P NR	1M PBS	7.32	Ni_2P NR	1M KOH	14.12
Ni_2P NR	3M H_2SO_4	-0.37	Ni_2P NR	6M KOH	15.36

Table S3. Comparison of HER performance in acidic solution for Ni_2P NR with other electrocatalysts

Catalyst	onset overpotential	Loading amounts (mg cm-^{2})	Current density (mA cm^{-2})	Overpotential (mV)	Tafel slope (mV dec^{-1})	Solution (H_2SO_4)	Ref
MoS_2/RGO		0.28	10	~150	41	0.5 M	[20]
MoS_2 NS		0.566	25	280	90	0.5 M	[21]
NiP_2 NS/CC		4.3	10	75	51	0.5 M	[22]
Ni_2P/C		0.36	10	87	54	0.5 M	[23]
Ni_2P/Ti		2	20	138	60	1 M	[24]
Ni_2P/CNS		0.857	10	174	64	0.5M	[25]
$NiSe_2$/Ni			10	143	49	0.5 M	[26]
Ni_5P_4-Ni_2P-NS			10	120	79.1	0.5 M	[27]
N-Co@G		0.285	10	265	98	0.5 M	[28]
CoP/CC	38	0.92	10	67	51	0.5 M	[29]
Co_2P on Ti foil	70	1.02	10	134	71	0.5 M	[21]
CoP–CNTs	64	0.19	10	139	52	0.5 M	[30]
MoP	40	0.36	10	125	54	0.5 M	[31]
WS_2 nanosheets	60	0.285	10	151	72	0.5 M	[32]
$CoSe_2$	45	0.037	10	231	42.4	0.5 M	[33]
Ni_2P NP	147	0.857	10	213	76	0.5 M	this work
Ni_2P NR	**27**	**0.857**	**10**	**127**	**54**	**0.5 M**	**this work**
Ni_2P NF	133	0.857	10	194	67	0.5 M	this work

Table S4. Comparison of HER performance in 1M KOH for Ni_2P NR with other electrocatalysts

Catalyst	Substrate	Mass loading (mg cm^{-2})	η_{10}（mV）	Tafel slope (mV dec^{-1})	Reference
NiS nanoparticles	Glassy carbon	0.283	474	124	[34]
NiS_2 nanoparticles	Glassy carbon	0.283	454	128	[34]
Ni_3S_2 nanoparticles	Glassy carbon	0.283	335	97	[34]
CoP	carbon cloth	0.92	209	129	[29]
FeP	Carbon cloth	1.5	218	146	[35]
Ni_2P	Ni foam	3.5	~	50	[6]
Ni_5P_4	Ti foil	177	49	98	[36]
MoP	Glassy carbon	0.86	~	48	[37]
CoO_x@CN	Glassy carbon	0.196	232	114	[38]
Co@N-C	Glassy carbon	0.196	210	108	[39]
Ni_2P NP	Glassy carbon	0.86	239	128	this work
Ni_2P NR	**Glassy carbon**	**0.86**	**169**	**78**	**this work**
Ni_2P NF	Glassy carbon	0.86	206	93	this work

Table S5. Comparison of OER performance for Ni_2P NR with some recently reported catalysts supported on different substrates in alkaline solution

Catalyst	Substrate	Electrolyte	η_{10}（mV）	Reference
NiCo	Glassy carbon	1M KOH	367	40
NiOx	Hematite substrate	1M KOH	360	41
CoN_4	Glassy carbon	1M KOH	330	42
Ni–Co PBA	Glassy carbon	1M KOH	380	43
$Co_3O_4/NiCo_2O_4$ Nanocages	Ni Foam	1M KOH	340	44
$NCNT/Co_xMn_{1-x}O$	Glassy carbon	1M KOH	340	45
single-unit-cell thick	Glassy carbon	1M KOH	370	46
S,S’-CNT	Graphite electrode	1M KOH	350	47
$ESM/CNTG/NiCo_2O_4$	Eggshell membrane	1M KOH	~370	48
$Ni_xCo_{3-x}O_4$	Glassy carbon	1M NaOH	~330	49
Amorphous CoSx porous nanocubes	Glassy carbon	1M KOH	290	50
Ni_2P NP	Glassy carbon	1M KOH	390	this work
Ni_2P NR	**Glassy carbon**	**1M KOH**	**320**	**this work**
Ni_2P NF	Glassy carbon	1M KOH	360	this work

4.1 Exposing surfaces of Ni_2P.

The most probable exposing crystal surfaces should be settled firstly in order to implement DFT calculation. As indicated by previous computational studies[51, 52, 53, 54], (001) crystalline surface in Ni_2P is usually imported as exposing surfaces. Also the existing of (001) surfaces are certified by HRTEM on Ref.51[55]. Two kinds of terminates are contained on (001) surfaces; this means that the Ni_3P-terminates (denoted as 001-Ni_3P-ter) and the Ni_3P_2-terminates (denoted as 001-Ni_3P_2-ter). To the best of our knowledge, the catalytic activities of the crystalline surfaces of the Ni_2P toward HER or OER have not yet been clarified. Therefore, a study is demanded on such possibilities.

In order to simply and generally figure out the possible exposing surfaces, the BFDH (Braviais-Friedel-Donnay-Harker) model proposed in early stage[56] has been introduced, which considered the growth rate (R) of a certain crystal surface (hkl) to be inversely proportion to the distance of atomic layers (d): $R \propto 1/d$. The atom with same z values forms an atomic layer, where z axis is set perpendicular to the associated surfaces (see Figure S23b). Based on this definition of atomic layer, the total growth rate of on a surface orientation should be marked as the average of $1/d$:

$$R_{hkl} = \frac{\sum_{i=1}^{n} 1/d_{hkl}^{i}}{n} \qquad \text{Eq.S1}$$

where n layers (n>5) are used to calculate the average value of R_{hkl}. d_i^{hkl} is the distance between layers on atomic layer i and i+1 along the crystal orientation (hkl). According to the BFDH model, the surfaces with the lower R_{hkl} are more facile to be conserved as the practical exposing surfaces. By Eq.S1, various basic crystal surfaces are studied, R_{hkl} values of which are listed on Figure S22. It is evident that atoms on 100, 001 and 110 surface have lower R_{hkl} than the other surfaces, suggesting their higher possibilities to expose. Among them, 110 surface are composed with only P atoms (insert on Figure S22), while 100 and 001 contain both P and Ni atoms. Since the interactions between P atoms are weaker than that between Ni and P, the surface energies of 110 surfaces should be lower than 001 and 110 surfaces. Likewise, lower surface energy of 110 is also supported by DFT calculation that formation energy of P on 110 surfaces are at least 1.1 eV more positive than that on 100 and 001 surfaces, indicating the unreferenced exposure for 110 surface. Therefore, in this paper, the surfaces of 001 (with 001-Ni_3P-ter and 001-Ni_3P_2-ter) and 100 are considered as the practical exposing surfaces of Ni_2P.

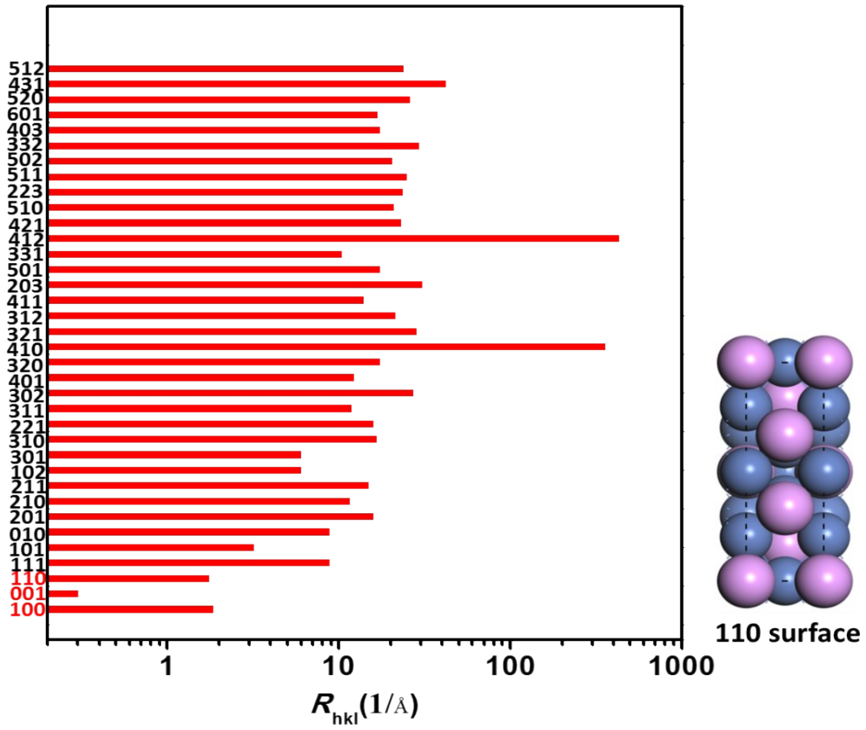

Figure S22 The values of R_{hkl} on different surfaces. The associated hkl values are displayed on the left, from which it is indicated that 110, 001 and 100 surfaces are the surfaces with the lowest growing rate. The insert gives the top views of 110 surface, which clearly indicates the exposing surfaces are contained only by P atoms.

4.2 “Detective pin” in screening the active adsorption site.

The associated PVP, H and O adsorption studied in this paper are then studied on surfaces of 001-Ni_3P-ter, 001-Ni_3P_2-ter and 100. As inferred by Ni_2P’s complex surface configuration and component, the active site for adsorption should be settled firstly. Since it is difficult to directly judge the active site, we here introduce a method we named the “detective pin”: 1. the united cell is divided uniformly by a 5×5 grid (see Figure S23c); 2. The “pin molecule” (O, H or PVP) is placed initially above the center of the first grid; 3. during the structure optimizing, the pin molecule is only allowed to relax on z direction with fixed x and y coordinates; 4. optimizing processes are implemented on each grid, so totally we have 5×5=25 optimized structures. Such method of detective pin can help to screen the sites with favorable adsorption energies for PVP, H and O. Then the characteristic of each active site is elaborated separately.

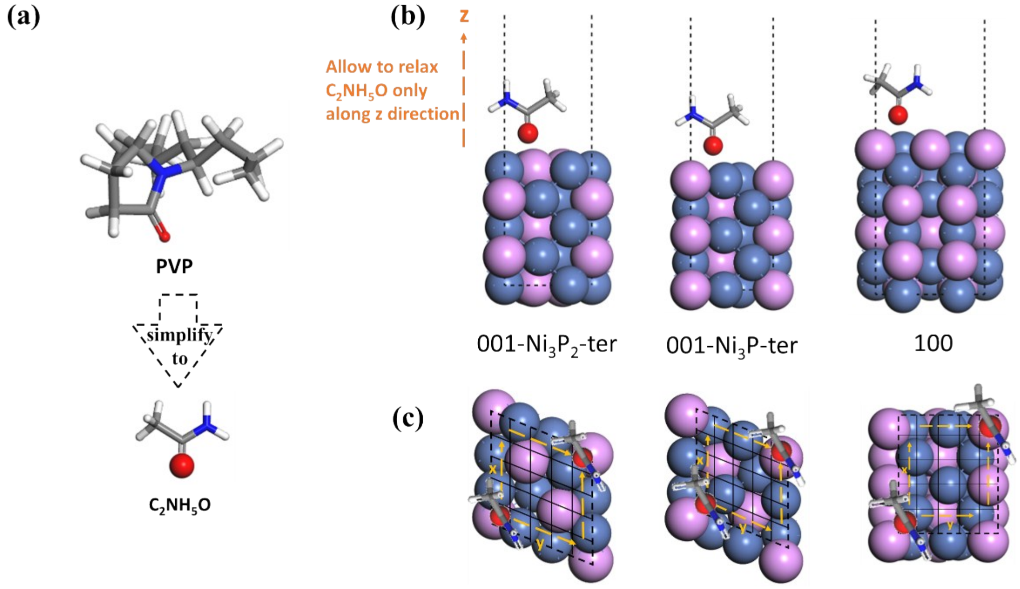

Figure S23 (a) The structure of PVP and its simplification group C_2NH_5O used in the model. (b) Side views of surface 001-Ni_3P-ter, 001-Ni_3P_2-ter and 100. (c) Top views of surface 001-Ni_3P-ter, 001-Ni_3P_2-ter and 100 with the 5×5 grid for detecting pin to locate. Dashed lines represent the united cells.

For PVP adsorption, we should first define the PVP structures used in the model: since PVP is a macromolecule with long carbon chains, it is speculated that only the carbonyl or tertiary amine contain the activities towards surfaces. And because the exposing of tertiary amine to surface will arise a large steric hindrance (based on its configuration on Figure S23a), the probable active group of PVP with Ni_2P surfaces would be the carbonyl. Inspired by this, the whole PVP structure is simplified by molecule C_2NH_5O (see Figure S23a).

The optimizing results of detective pin on three surfaces are shown on Figure S24, where the colors on each grid represent the adsorption energies. The more negative adsorption energies (means more stable) are painted by blue, while the more positive adsorption energies (means less stable) are pained by red. Hence the sites with deepest blue represent the most active sites. Similarly, the results of O* and H* adsorption are also given on Figure S24.

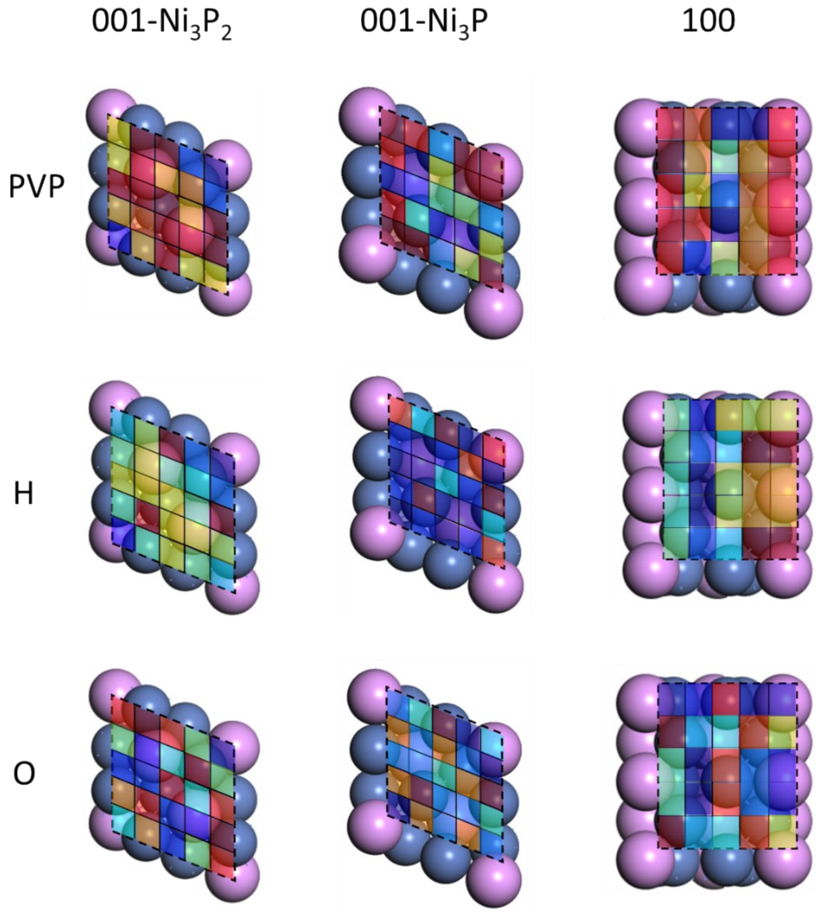

Figure S24 The results of the detector pins of PVP, H and O on three associated surfaces. The colors can reflect their optimized energies, where blue and red indicate the strong and weak adsorption, respectively, from which we can rapidly figure the active sites for associated surfaces and adsorbates.

Afterwards, by re-optimizing x, y and z coordinates of the associated PVP above the sites painted by deepest blue, the associated adsorption energies of PVP, H and O on 001 and 100 surface are obtained.

4.3 HER and OER activities on each site

To explain the electrocatalysis of HER, the value of ΔG_{H*} (H* adsorption Gibbs energy) is usually imported as an effective activity descriptor for the exchange current density[57, 58]. However, for the HER of Ni_2P, with relatively large onset overpotential, the surface (H* coverage) of catalysts is deviated from that on equilibrium potential so that implementing the descriptor ΔG_{H*} here is not a rigorous choice. As an alternative method used in this paper, we directly calculate the kinetic current of HER on Ni_2P.

To calculate the kinetic current of HER, as deduced by the Tafel slope demonstrated in the main body, the HER goes through the Heyrovsky-Volmer pathway, which is expressed as follows (* is the blank sites on the given surfaces):

$H^{+}+e+* \rightarrow H*$ Volmer RS1

$H*+ H^{+}+e \rightarrow H_2+*$ Heyrovksy RS2

And Heyrovsky reaction is considered to be the rate-limiting step based on its Tafel slope (see Figure 3b and the discussion on the main text) so that Volmer reaction is assumed to be in equilibrium. Under this situation, based on the derivation on Ref.59, the exchange current density contributed by a site marked as *i* on Ni_2P surface is expressed as:

$$j_i^0 = Fk_0\theta_i^\alpha(1-\theta_i)^{1-\alpha} \qquad \text{S2}$$

where α is symmetrical coefficient; θ_i is the H* coverage of site *i*. With the Bulter-Volmer equation, the kinetic current on any given overpotential η is expressed as:

$$j_i = j_i^0[\exp(\frac{\alpha nF\eta}{RT}) - \exp(-\frac{(1-\alpha)nF\eta}{RT})] \qquad \text{S3}$$

where *n* is the total number of charge transfer (*n*=2 for HER); *F* is the Faraday constant. Combine Eq.S2 with S3, assume α to be 0.5 and use U_RHE (potential vs RHE) in replace of η, we have

$$j_i = k_0F\theta_i^{0.5}(1-\theta_i)^{0.5}[\exp(-\frac{U_\text{RHE}e}{RT}) - \exp(\frac{U_\text{RHE}e}{RT})] \qquad \text{S4}$$

The coverage of site *i* can be derived by the equilibrium of Volmer reaction:

$$\Delta G^\text{RS1} = 0 = G_0^\text{H*-i} - \frac{1}{2}G_0^\text{H2} + RT\ln\frac{\theta_i}{1-\theta_i} + U_\text{RHE}e \qquad \text{S5}$$

where G_0^H2 is the standard Gibbs free energy of solvated H_2 (with a concentration of 1 mol/L); $1/2G_0^\text{H2}$ is the replacement of $G_0^\text{H+}$ for reaction $H_2 \rightarrow 2H^+ + 2e$ are equilibrium on U_RHE=0 V. Term $\text{RTln}\theta/(1-\theta)$ is the configuration entropy under mean field approximation. $G_0^\text{H*-i}$ is the standard adsorption Gibbs free energy of H* on site *i*, which can be directly calculated by combination of DFT-based H* adsorption energy and its zero point energy (ZPE) and entropy ($G_0^\text{H*-i} = E_\text{DFT}^\text{H*-i-slab} - E_\text{DFT}^\text{slab} + \text{ZPE}_\text{H*} - \text{TS}_\text{H*}$). Yet considering the deviation of physical environment (like the charge, electric field) exists between DFT model and experimental electrode interface, such DFT-based $G_0^\text{H*-i}$ is with inaccuracy. Hence the value of θ_i is deviated as well calculated by Eq.S5. In cope with this, instead of the absolute value, it is better to use the relative H* adsorption energy with respect to that on Pt (111) ($G_0^\text{H*-i} - G_0^\text{H*-Pt111}$). With this idea, we write the equilibrium function of Volmer reaction on Pt (111) surfaces:

$$U_{\mathrm{RHE}}e=-G_0^{\mathrm{H^*\text{-}Pt}}(\theta_{\mathrm{H^*\text{-}Pt}})+\frac{1}{2}G_0^{\mathrm{H_2}}-RT\ln\frac{\theta_{\mathrm{H^*\text{-}Pt}}}{1-\theta_{\mathrm{H^*\text{-}Pt}}} \qquad \text{S6}$$

(note $G_0^{\mathrm{H^*\text{-}i}}$ on Eq.S5 is independent with coverage, while $G_0^{\mathrm{H^*\text{-}Pt}}$ on Eq.S6 is not. The reason is that usually the sites on Ni_2P are separated and have tiny interaction so that they are coverage independent, while a much shorter distance between sites exists on Pt(111) surface, which leads to a coverage dependent adsorption energy, or namely, the isotherm). Then we choose the 0.5 ML of $\theta_{\mathrm{H^*\text{-}Pt}}$ along with its corresponding U_{RHE} that is inferred by experimental CV (0.07 V on pH=1 and 0.16 V on pH=13 from ref.56). Then takes that into Eq.S6. Afterwards, Eq.S5 minus Eq.S6 gives:

$$0=-G_0^{\mathrm{H^*\text{-}i}}+G_0^{\mathrm{H^*\text{-}Pt}}(\theta_{\mathrm{H^*\text{-}Pt}}=0.5)-RT\ln\frac{\theta_i}{1-\theta_i} \qquad \text{S7}$$

where $G_0^{\mathrm{H^*\text{-}i}}$-$G_0^{\mathrm{H^*\text{-}Pt}}(\theta_{\mathrm{H^*\text{-}Pt}}=0.5)$ can be calculated approximately by their DFT-based adsorption energy differences: $G_0^{\mathrm{H^*\text{-}i}}-G_0^{\mathrm{H^*\text{-}Pt}}(\theta_{\mathrm{H^*\text{-}Pt}}=0.5)\approx E_{\mathrm{0\text{-}DFT}}^{\mathrm{H^*\text{-}i}}-E_{\mathrm{0\text{-}DFT}}^{\mathrm{H^*\text{-}Pt}}(\theta_{\mathrm{H^*\text{-}Pt}}=0.5)$. Hence by Eq.S7 we can have the θ_{i} under the U_{RHE}=0.07 V on pH=1 and U_{RHE}=0.16 V on pH=13. Takes that into the Eq.S5, we obtain the value of $-G_0^{\mathrm{H^*\text{-}i}}+1/2G_0^{\mathrm{H2}}$. As a consequence, by Eq.S5 we can finally have the θ_i value under any given U_{RHE}. Within the U_{RHE} dependent θ_i value, HER activities (represented by the current) can be calculated by Eq.S4. In addition, since the k_0s and Fs on Eq.S4 are equal for each site i and only the relative value of current on each site really matters, the value of Fk_0 is to be 1.

As for OER activity, similar method with Ref.50 is proposed that we use the value of general OER descriptor $\Delta G_{\mathrm{O^*}}$-$\Delta G_{\mathrm{OH^*}}$[60] with respect to RuO_2 that commonly considered to be the best catalyst.

4.4 Details of DFT calculation

Spin-polarized DFT calculations were performed with periodic super-cells under the generalized gradient approximation (GGA) using the Perdew-Burke-Ernzerhof (PBE) functional for exchange-correlation and the ultrasoft pseudopotentials for nuclei and core electrons. The Kohn-Sham orbitals were expanded in a plane-wave basis set with a kinetic energy cutoff of 30 Ry and the charge-density cutoff of 300 Ry. The Fermi-surface effects has been treated by the smearing technique of Methfessel and Paxton, using a smearing parameter of 0.02 Ry. Periodically repeated slab model with 001-Ni_3P_2-ter, 001-Ni_3P-ter and 100 surfaces are introduced (the side views of which are shown on Figure S23), while half of the topmost layers are allowed to relax during the structure optimization until the Cartesian force components acting on each atom were below 10^{-3} Ry/Bohr and the total energy converged to within 10^{-5} Ry. The Brillouin-zones were sampled with a 5×5×1 k-point mesh. The PWSCF codes contained in the Quantum ESPRESSO distribution[61] were used to implement the calculations.

5. Analysis on the exposing surfaces with the influence of PVP.

The results of the adsorption energies show that it is thermodynamically favorable for PVP adsorption on all the studied surfaces (adsorption energies are calculated to be -0.23 eV, -0.26 eV and -0.15 eV on 001-Ni_3P_2-ter, 001-Ni_3P-ter and 100 surfaces, respectively), from which it is indicated PVP can interact with all these three surfaces, while PVP affinity is much higher on 001 with 0.1 eV more favorable in adsorption energy. And the adsorption energies on 001-Ni_3P_2-ter and 001-Ni_3P-ter are similar so that PVP may not have the adsorption preference of these two terminates on 001. As a consequence, during the growth of PVP concentration, PVP firstly adsorbs on 001 surface, then on 100 surface. Under this framework, in order to quasi-quantitatively study the Ni_2P morphologies driven by PVP concentration, we assume the adsorption of PVP follows chemical function as PVP(sol)+*→PVP*, which leads to the following expression:

$$\Delta G = 0 = G^{0}_{\text{PVP-ad}} - G_{\text{PVP}} + RT\ln\frac{\theta_{\text{PVP*}}}{1-\theta_{\text{PVP*}}} \qquad \text{Eq.S8}$$

where G^{0}_{PVP}-ad is the Gibbs free energy of adsorbed PVP monomer and G_{PVP} is the Gibbs free energy of PVP monomer (C_2NH_5O) on solvation. G^{0}_{PVP}-ad is dependent with surfaces. G_{PVP} is dependent with PVP concentration c_{PVP} by $G_{\text{PVP}}=G^{0}_{\text{PVP}}+\text{RTln}c_{\text{PVP}}$ (G^{0}_{PVP} is the standard formation Gibbs energy of solvated PVP). $RT\ln(\theta_{\text{PVP*}}/1-\theta_{\text{PVP*}})$ is the configurational entropy under mean field approximation. From Eq.S2 we can derive the expression of PVP coverage:

$$\theta_{\mathrm{PVP}} = \frac{1}{\exp(-\frac{G_{\mathrm{PVP}} - G^{0}_{\mathrm{PVP\text{-}ad}}}{RT}) + 1} \qquad \text{Eq.S9}$$

Then approximately, the $G^0{}_{\mathrm{PVP\text{-}ad}}$ difference between 001 and 100 surfaces equates their adsorption energy:

$G^0{}_{\mathrm{PVP\text{-}ad}}(001)\text{-}G^0{}_{\mathrm{PVP\text{-}ad}}(100) \approx E^0{}_{\mathrm{PVP\text{-}ad}}(001)\text{-}E^0{}_{\mathrm{PVP\text{-}ad}}(100)=-0.1$ eV   Eq.S10

Hence if we portray a curve with θ as vertical axis and $G_{\mathrm{PVP\text{-}ad}}\text{-}G^0{}_{\mathrm{PVP}}$ as horizontal ordinate, the isotherm curve of PVP adsorption on 100 (red curve on Figure S25) should locate 0.1 eV more positive than the curves of PVP adsorption on 001 (black curve on Figure S25). By Figure S25, once the concentration of PVP is known, the value of $G_{\mathrm{PVP}}\text{-}G^0{}_{\mathrm{PVP\text{-}ad}}$ is achieved immediately, then the ratio of PVP coverage on 100 to 001 surfaces is settled. Under this framework, we can understand the key role of PVP concentration with the help of Figure S25: on low concentration of PVP (dashed orange line on the left), 100 and 001 surfaces are occupied with the similar low coverage (~ 0 ML) of PVP; on high concentration of PVP (dashed orange line on the right), 100 and 001 surfaces are occupied with the similar high coverage (~ 1 ML) of PVP; on medium concentration of PVP (dashed orange line in the middle), obvious distinction exists that PVP coverage on 001 surface are far larger than that on 100 surface. Since PVP is a macromolecule with a long carbon chain, its adsorption hinders the further deposition of Ni and P ion, which then constrains the growth of crystal on corresponding orientation. Therefore, on medium PVP concentration, the crystal growth along 001 orientation are hindered, while that on 100 surfaces is with a larger growth rate, resulting in much larger amount conservation of 001 surfaces than

100 surfaces (growth of surfaces extinguishes their exposures). For high and low PVP concentrations, such PVP hinder effects are similar, leading to the similar exposing ratio of these two surfaces. On the basis of this, we deduced a Ni_2P NR formation mechanism adjusted by optimized concentration of PVP and portrayed that on Figure S26.

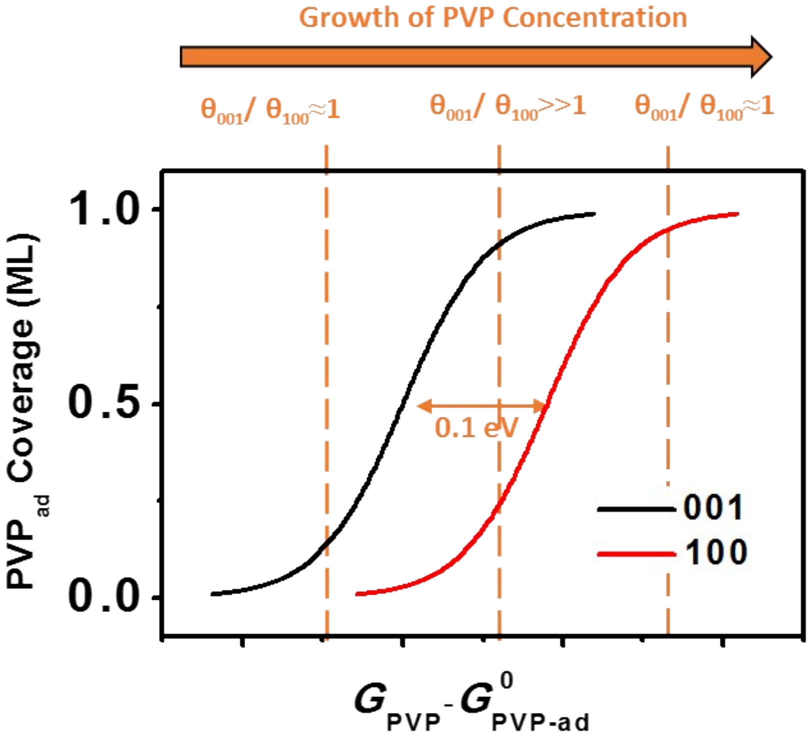

Figure S25 The quasi-quantitative analysis of ratio of PVP coverage on 001 (θ_{001}, black curve) to 100 (θ_{100}, red curve). Three dashed lines display three different PVP coverage ratios driven by three different PVP concentrations (concentration grows from left to right). The left (right) dashed line represents the situation when the PVP concentration is low (high) and the both very low (high) values of θ_{001} and θ_{100} lead by it. Under this circumstance, PVP concentration will appear no preference of adsorption on 100 and 001 surfaces. Contrarily, the medium dashed line reveals the situation where θ_{001} and θ_{100} are highly distinct, indicating that medium PVP concentration will cause far larger PVP* coverage on 001 surface than on 100 surface.

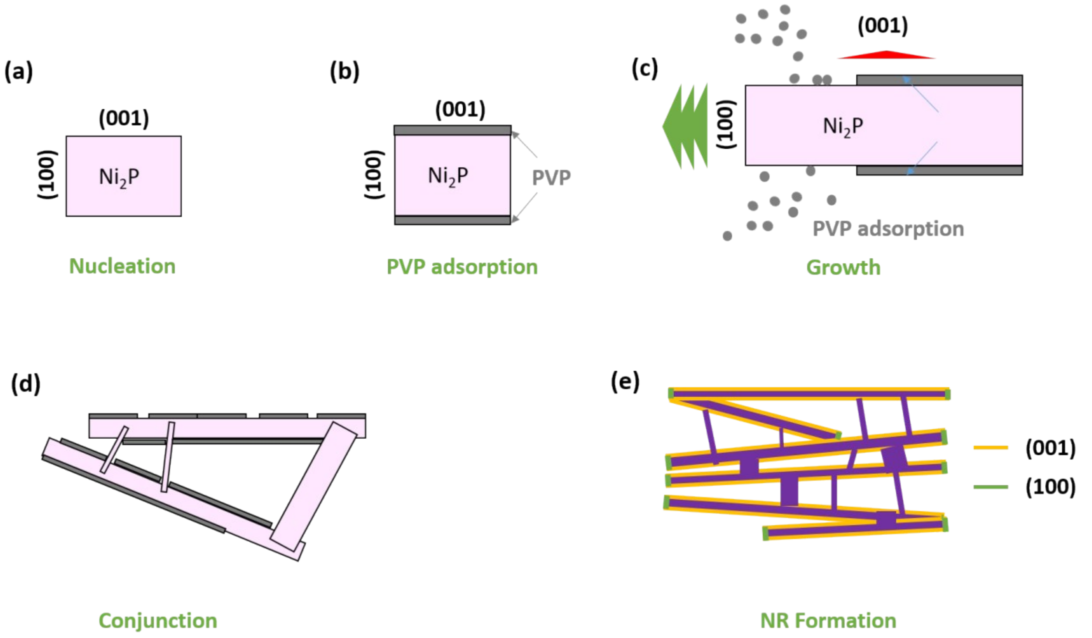

Figure S26. The scheme of the Ni$_2$P NR formation process under optimized PVP concentration. (a) The nucleation process. A small nuclear is formed by Ni and P ion. (b) PVP adsorption. Notice on optimized PVP concentration, PVP prefers to adsorb on 001 surface, with very low coverage on 100 surface. (c) The growth process. With the protection of PVP, the growth rate on 001 orientation is slow, while that on 100 orientation is much faster, leading to the conservation of 001 surface. (d) The conjunction process. Rods met during the growth. Since the PVP adsorption is a kinetic process, leaving some areas of 001 surface that is uncovered by PVP. Then the deposition of Ni and P ions on these area form the conjunctions that connect the neighboring rods. Such conjunctions appear universally. (e) NR formation process, in which a 2-dementional scheme is portrayed. Eventually, the NR with rods and conjunctions will be yield with highly exposed 001 surface and much lower exposed 100 surfaces.

6. **HER activities**

The preferred sites of H* adsorption are given on Figure S27a, from which the adsorption order is marked by numbers. It is worth to note the dashed circled site 1 on each surface suggests the site that is preliminary to adsorb, yet during the further adsorption, H* on dashed circled site 1 will be repulsed to the site on the solid circle. The coverage and the current contribution are given on Figure S27b-c for pH=1 and S27d-e for pH=13. The current results of Figure S27c & e are intuitive, while the coverage results on Figure S24b & d can be understood by that a site with a coverage more close to 0.5 ML is more active (indicated by Eq.S4). And the coverage more close to ~1 and 0 ML indicate the adsorption on the associated site are too strong and too weak for catalyzing HER, respectively. Figure S27b-d indicated that among all the sites on these three surfaces, dashed circled 001-Ni_3P-ter-site1 seems to domain the current for HER both on pH=1 and 13. The other sites are all inactive or poisoned by H* with the coverage approaching to 1 or 0 ML, expect for 100-site2 which has some H* adsorption on acid electrolyte.

This results suggest 001-Ni_3P-ter surfaces are the most active surface among the three surfaces with 001-Ni_3P-site1 as the most active site of HER. On the basis of this, we can understand the enhancement effect of HER activities caused by the optimized PVP concentration is originated from the more exposed 001 surfaces rendered by it.

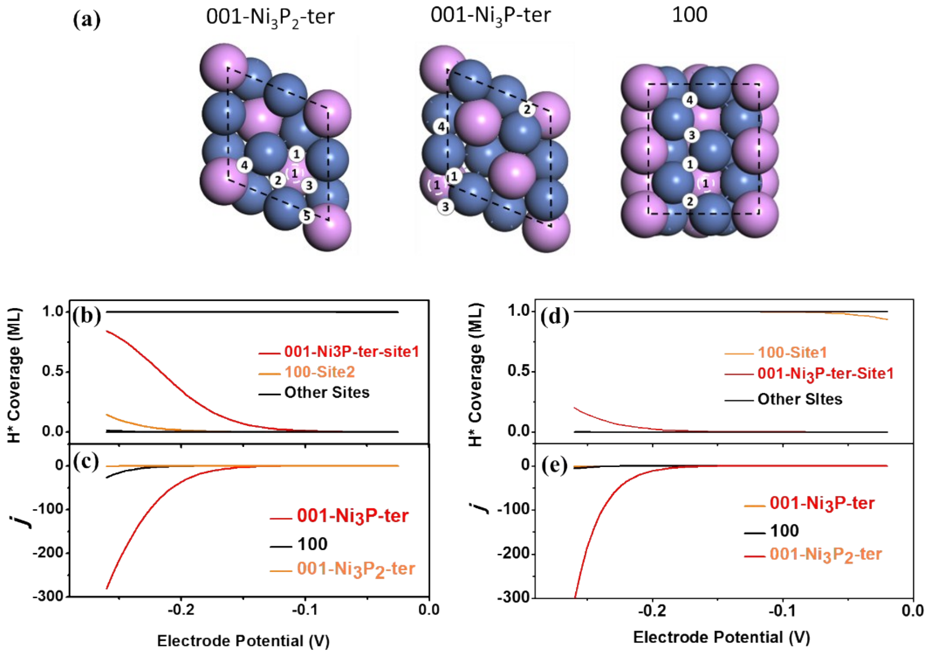

Figure S27 (a) H* adsorption site. The adsorption order is marked by the numbers. The dashed number 1 is the site for first H* adsorption. Then with further H* adsorption, the H* is repulsed to the site marked by solid circle. (b) – (d) give the H* coverage (calculated by Eq.S8) and the value of *j* (calculated by Eq.S7), where the situation on pH=1 and pH=13 are shown on (b) – (c) and (d) – (e), respectively. Note we ignore the unit of the currents on c and e for its absolute value is meaningless since we have set k^0F=1.

Table S6 The calculated H* adsorption energies on associated site denoted on Figure S24a. All the values are in reference with the H* adsorption on Pt (111) surface with a coverage of 0.5 ML ($G_0^{H*\text{-}i}$-$G_0^{H*\text{-}Pt}$($\theta_{H*\text{-}Pt}$=0.5)). The location of each site is show on Figure S24a. (unit: eV)

Site	001-Ni_3P_2-ter	001-Ni_3P-ter	100
1	-0.569	-0.067	-0.411
2	0.151	0.173	0.023
3	0.293	0.081	0.354
4	0.465	0.179	0.492
5	--	0.911	--

7. OER activities

For OER, the calculated results of ΔG_{O*}-ΔG_{OH*} (the value is with respect to top of OER activity volcano) on each site are listed on Table S7 and Figure S28. It is implied from Figure S28 and Table S7 that the all the associated sites locate on the right brunch of OER volcano plot, suggesting the oxidation of these sites during OER is weak so that all the three surfaces can keep its original configuration during OER. This makes the straightforward comparison of ΔG_{O*}-ΔG_{OH*} on each site meaningful, from which it is indicated the 001-Ni_3P-ter-site1-Ox (shown on Figure S28, notice: not the same site as HER) is the most active site for OER. Meanwhile, the activity of 001-Ni_3P-ter-site1-Ox is far larger than the other sites on all surfaces. For example, the second most active site is 001-Ni_3P_2-ter-site1-Ox and possesses a 0.2 eV more positive value of ΔG_{O*}-ΔG_{OH*} than 001-Ni_3P-site1. These deviation actually means as large as 0.2 V higher overpotential (Figure S28b) on the basis of the meaning of theoretical volcano plot[60]. These results explain the reason why Ni_2P has OER activity. Likewise, this again confirms that the 001-Ni_3P-ter surface is the most active surface, which also indicates the benefit of optimized concentration of PVP. Besides, we found that the active site for OER is different from that for HER.

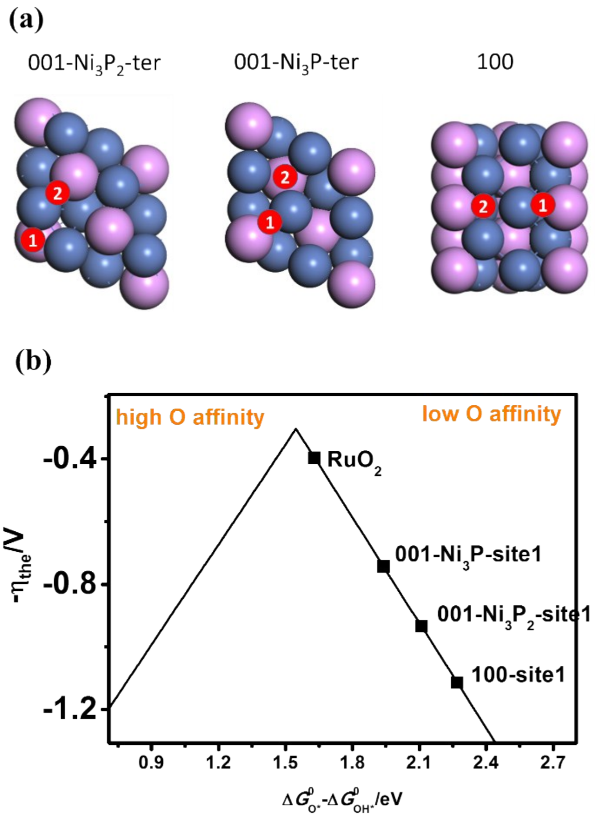

Figure S28. (a) The optimized adsorption sites on three associated surfaces. The number indicates the adsorption order based on their adsorption energies. (b) The values of OER activity descriptor ΔG_{O*}-ΔG_{OH*} of each site and their associated location on theoretical volcano plot referred from Ref.13. The adsorption of the other sites marked on (a) is too weak so that we ignore them on the volcano plot.

Table S7 The values of ΔG_{O*}-ΔG_{OH*} with respect to the top of OER volcano activity plot from Ref.60. The associated numbers represent the sites on Figure S28. (unit: eV)

Site number	001-Ni_3P_2	001-Ni_3P	100
1	0.56	0.39	0.72
2	1.14	1.16	1.21

Reference

1. M. Gao, W. Sheng, Z. Zhuang, Q. Fang, S. Gu, J. Jiang and Y. Yan, Journal of the American Chemical Society, 2014, 136, 7077-7084.
2. Y. Pan, Y. Liu, J. Zhao, K. Yang, J. Liang, D. Liu, W. Hu, D. Liu, Y. Liu and C. Liu, J. Mater. Chem. A, 2015, 3, 1656-1665.
3. Y. Zhao, Y. Zhao, H. Feng and J. Shen, Journal of Materials Chemistry, 2011, 21, 8137.
4. S. Sawhill, K. Layman, D. Vanwyk, M. Engelhard, C. Wang and M. Bussell, Journal of Catalysis, 2005, 231, 300-313.
5. T. I. Korányi, Applied Catalysis A: General, 2003, 239, 253-267.
6. Y. Shi, Y. Xu, S. Zhuo, J. Zhang and B. Zhang, ACS applied materials & interfaces, 2015, 7, 2376-2384.
7. Y. Li, H. Wang, L. Xie, Y. Liang, G. Hong and H. Dai, Journal of the American Chemical Society, 2011, 133, 7296-7299.
8. Z. Huang, Z. Chen, Z. Chen, C. Lv, M. G. Humphrey and C. Zhang, Nano Energy, 2014, 9, 373-382.
9. P. Jiang, Q. Liu and X. Sun, Nanoscale, 2014, 6, 13440-13445.
10. Y. Bai, H. Zhang, X. Li, L. Liu, H. Xu, H. Qiu and Y. Wang, Nanoscale, 2015, 7, 1446-1453.
11. Z. Pu, Q. Liu, C. Tang, A. M. Asiri and X. Sun, Nanoscale, 2014, 6, 11031-11034.
12. Y. Li, P. Cai, S. Ci and Z. Wen, ChemElectroChem, 2017, 4, 340-344.
13. H. Zhou, Y. Wang, R. He, F. Yu, J. Sun, F. Wang, Y. Lan, Z. Ren and S. Chen, Nano Energy, 2016, 20, 29-36.
14. X. Wang, Y. V. Kolen'ko, X. Q. Bao, K. Kovnir and L. Liu, Angewandte Chemie, 2015, 54, 8188-8192.
15. H. Fei, Y. Yang, Z. Peng, G. Ruan, Q. Zhong, L. Li, E. L. Samuel and J. M. Tour, ACS applied materials & interfaces, 2015, 7, 8083-8087.
16. J. Tian, Q. Liu, A. M. Asiri and X. Sun, Journal of the American Chemical Society, 2014, 136, 7587-7590.
17. C. Wu, Y. Yang, D. Dong, Y. Zhang and J. Li, Small, 2017, 13.
18. Z. Xing, Q. Liu, A. M. Asiri and X. Sun, Advanced materials, 2014, 26, 5702-5707.
19. Z. Wu, B. Fang, A. Bonakdarpour, A. Sun, D. P. Wilkinson and D. Wang, Applied Catalysis B: Environmental, 2012, 125, 59-66.
20. D. Kong, J. J. Cha, H. Wang, H. R. Lee and Y. Cui, Energy & Environmental Science, 2013, 6, 3553.
21. N. Jiang, Q. Tang, M. Sheng, B. You, D.-e. Jiang and Y. Sun, Catal. Sci. Technol., 2015, DOI: 10.1039/c5cy01111f.
22. Y. Liang, Q. Liu, A. M. Asiri, X. Sun and Y. Luo, ACS Catalysis, 2014, 4, 4065-4069.
23. A. B. Laursen, K. R. Patraju, M. J. Whitaker, M. Retuerto, T. Sarkar, N. Yao, K. V. Ramanujachary, M. Greenblatt and G. C. Dismukes, Energy & Environmental Science, 2015, 8, 1027-1034.
24. P. Xiao, M. A. Sk, L. Thia, X. Ge, R. J. Lim, J.-Y. Wang, K. H. Lim and X. Wang, Energy Environ. Sci., 2014, 7, 2624-2629.
25. H. Jin, J. Wang, D. Su, Z. Wei, Z. Pang and Y. Wang, J. Am. Chem. Soc, 2015, 137, 2688-2694.

26. J. Wang, D. Gao, G. Wang, S. Miao, H. Wu, J. Li and X. Bao, J. Mater. Chem. A, 2014, 2, 20067-20074.
27. H. Liang, F. Meng, M. Caban-Acevedo, L. Li, A. Forticaux, L. Xiu, Z. Wang and S. Jin, Nano letters, 2015, 15, 1421-1427.
28. K. Fominykh, J. M. Feckl, J. Sicklinger, M. Döblinger, S. Böcklein, J. Ziegler, L. Peter, J. Rathousky, E.-W. Scheidt, T. Bein and D. Fattakhova-Rohlfing, Advanced Functional Materials, 2014, 24, 3123-3129.
29. P. Chen, K. Xu, Y. Tong, X. Li, S. Tao, Z. Fang, W. Chu, X. Wu and C. Wu, Inorg. Chem. Front., 2016, 3, 236-242.
30. L. Han, X. Y. Yu and X. W. Lou, Advanced materials, 2016, 28, 4601-4605.
31. H. Hu, B. Guan, B. Xia and X. W. Lou, Journal of the American Chemical Society, 2015, 137, 5590-5595.
32. X. Liu, M. Park, M. G. Kim, S. Gupta, X. Wang, G. Wu and J. Cho, Nano Energy, 2016, 20, 315-325.
33. L. Liang, H. Cheng, F. Lei, J. Han, S. Gao, C. Wang, Y. Sun, S. Qamar, S. Wei and Y. Xie, Angewandte Chemie, 2015, 54, 12004-12008.
34. A. M. El-Sawy, I. M. Mosa, D. Su, C. J. Guild, S. Khalid, R. Joesten, J. F. Rusling and S. L. Suib, Advanced Energy Materials, 2016, 6, 1501966.
35. J. Geng, H. Wu, A. M. Al-Enizi, A. A. Elzatahry and G. Zheng, Nanoscale, 2015, 7, 14378-14384.
36. Y. Li, P. Hasin and Y. Wu, Advanced materials, 2010, 22, 1926-1929.
37. P. Cai, J. Huang, J. Chen and Z. Wen, Angewandte Chemie, 2017, DOI: 10.1002/anie.201701280.
38. B. You, N. Jiang, M. Sheng, M. W. Bhushan and Y. Sun, ACS Catalysis, 2016, 6, 714-721.
39. Y. Jin, H. Wang, J. Li, X. Yue, Y. Han, P. K. Shen and Y. Cui, Advanced materials, 2016, 28, 3785-3790.
40. H. Liang, A. N. Gandi, D. H. Anjum, X. Wang, U. Schwingenschlögl and H. N. Alshareef, Nano letters, 2016, DOI: 10.1021/acs.nanolett.6b03803.
41. M. Kuang, P. Han, Q. Wang, J. Li and G. Zheng, Advanced Functional Materials, 2016, DOI: 10.1002/adfm.201604804.
42. M. Ledendecker, S. Krick Calderon, C. Papp, H. P. Steinruck, M. Antonietti and M. Shalom, Angewandte Chemie, 2015, 54, 12361-12365.
43. J. Li, M. Yan, X. Zhou, Z.-Q. Huang, Z. Xia, C.-R. Chang, Y. Ma and Y. Qu, Advanced Functional Materials, 2016, 26, 6785-6796.
44. L.-A. Stern, L. Feng, F. Song and X. Hu, Energy Environ. Sci., 2015, 8, 2347-2351.
45. J. Wang, H. X. Zhong, Z. L. Wang, F. L. Meng and X. B. Zhang, ACS Nano, 2016, 10, 2342-2348.
46. Y. Wu, G.-D. Li, Y. Liu, L. Yang, X. Lian, T. Asefa and X. Zou, Advanced Functional Materials, 2016, 26, 4839-4847.
47. Y. P. Zhu, T. Y. Ma, M. Jaroniec and S. Z. Qiao, Angewandte Chemie, 2016, DOI: 10.1002/anie.201610413.
48. C. Tang, N. Cheng, Z. Pu, W. Xing and X. Sun, Angewandte Chemie, 2015, 54, 9351-9355.
49. Y. Hou, Z. Wen, S. Cui, S. Ci, S. Mao and J. Chen, Advanced Functional Materials, 2015, 25, 872-882.
50. J. Luo, D. A. Vermaas, D. Bi, A. Hagfeldt, W. A. Smith and M. Grätzel, Advanced Energy Materials, 2016, 6, 1600100.

51. P. Liu and J. A. Rodriguez, Journal of the American Chemical Society, 2005, 127, 14871-14878.
52. P. Liu, J. A. Rodriguez, T. Asakura, J. Gomes and K. Nakamura, The Journal of Physical Chemistry B, 2005, 109, 4575-4583.
53. J. Ren, C.-F. Huo, X.-D. Wen, Z. Cao, J. Wang, Y.-W. Li and H. Jiao, The Journal of Physical Chemistry B, 2006, 110, 22563-22569.
54. J.-S. Moon, E.-G. Kim and Y.-K. Lee, Journal of Catalysis, 2014, 311, 144-152.
55. E. J. Popczun, J. R. McKone, C. G. Read, A. J. Biacchi, A. M. Wiltrout, N. S. Lewis and R. E. Schaak, Journal of the American Chemical Society, 2013, 135, 9267-9270.
56. J. D. H. Donnay and D. Harker, Am. Mineral, 1937, 22, 446-467.
57. J. K. Nørskov, T. Bligaard, A. Logadottir, J. Kitchin, J. G. Chen, S. Pandelov and U. Stimming, Journal of The Electrochemical Society, 2005, 152, J23-J26.
58. E. Skúlason, V. Tripkovic, M. E. Björketun, S. Gudmundsdottir, G. Karlberg, J. Rossmeisl, T. Bligaard, H. Jónsson and J. K. Nørskov, The Journal of Physical Chemistry C, 2010, 114, 18182-18197.
59. F. Yang, Q. Zhang, Y. Liu and S. Chen, The Journal of Physical Chemistry C, 2011, 115, 19311-19319.
60. I. C. Man, H. Y. Su, F. Calle‐Vallejo, H. A. Hansen, J. I. Martínez, N. G. Inoglu, J. Kitchin, T. F. Jaramillo, J. K. Nørskov and J. Rossmeisl, ChemCatChem, 2011, 3, 1159-1165.
61. Q. ESPRESSO, J. Phys.: Condens. Matter, 2009, 21, 395502.